Desalination and Water Treatment
www.deswater.com
doi: 10.5004/dwt.2021.26760

216 (2021) 14–33
March

Experimental study on the potential of combining TiO_2, ZnO, and Al_2O_3 nanoparticles to improve the performance of a double-slope solar still equipped with saline water preheating

Francisco Carranza[a,b,*], Claudia-Daniella Villa[c], José Aguilar[a], Hugo A. Borbón-Nuñez[b,d], Daniel Sauceda[a]

[a]*Renewable Energy Laboratory, Applied Physics Division, Centre for Scientific Research and Higher Education of Ensenada (CICESE), Hwy. Ensenada – Tijuana 3918, Zona Playitas, 22860, Ensenada, B. C. Mexico, Tel. +52 646 175 0500; emails: fcarranza@cicese.edu.mx (F. Carranza), aguilarj@cicese.edu.mx (J. Aguilar), dsauceda@cicese.edu.mx (D. Sauceda)*
[b]*National Council for Science and Technology (CONACYT), Insurgentes Sur Ave. 1582, Mexico City, 03940, Mexico, email: hborbon@cnyn.unam.mx (H.A. Borbón-Nuñez)*
[c]*Faculty of Engineering, Architecture and Design, Autonomous University of Baja California (UABC), Hwy. Ensenada – Tijuana 3917, Zona Playitas, 22860, Ensenada, B. C. Mexico, email: daniella.villa@uabc.edu.mx*
[d]*Center of Nanosciences and Nanotechnology, National Autonomous University of Mexico (CNyN UNAM), Hwy. Ensenada – Tijuana km. 107, Zona Playitas, 22860, Ensenada, B. C. Mexico*

Received 1 June 2020; Accepted 5 November 2020

ABSTRACT

Solar stills are an excellent option for providing freshwater to isolated communities living near the coast of Baja California, Mexico, and facing scarcity. Double-slope solar stills are simple and easy to operate; however, they normally produce low volumes of condensate. To overcome this, changes to the architecture of the still, implementation of mechanical items, or addition of nanoparticles to the water have been proposed. Since coupling the still with a solar water preheater and adding nanomaterials can be done without incurring in costly designs, and provided that using two types of nanoparticles simultaneously has the potential to further enhance the heat transfer capabilities, these options were investigated here. A spiral solar heater, utilized to increase the feedwater temperature, and combinations of TiO_2, ZnO, and Al_2O_3 nanoparticles were implemented to augment the yield of a double-slope solar still. The nanostructures were specifically synthesized for this application and experiments were done at the climate of Ensenada, Baja California. Nanostructures whose shape allowed wide contact with the water and with adequate absorptivity were produced. Peak yields and efficiencies of 5.46 L/m^2 and 59.9% were achieved combining TiO_2 + Al_2O_3, and 4.72 L/m^2 and 50.2% with TiO_2 + ZnO at costs between 0.034 and 0.038 US\$/L.

Keywords: Seawater desalination; Solar still; Nanotechnology; Metal oxide nanoparticles; Heat transfer

1. Introduction

1.1. Water scarcity scenario in Baja California, Mexico

According to the most recently published statistics of the National Water Commission of Mexico (CONAGUA), in 2018 the northern and arid state of Baja California (BC), Mexico, presented a freshwater availability of 849 m^3/cap/y [1]. This number is considerably lower than the minimum limit of 1,700 m^3/cap/y recommended by the United Nations for a country or region to meet its water necessities [2]. Whilst the two most populated cities of the state, Tijuana

* Corresponding author.

and Mexicali, satisfy their needs from the Colorado River and nearby aquifers; the third largest city, Ensenada, faces important shortage periods every year because the supply it receives from the same river is variable and often insufficient [3,4]. Furthermore, the majority of the local aquifers is overexploited or presents saline intrusion due to their closeness to the sea [1].

As an answer to the problem, a reverse osmosis (RO) desalination plant with capacity of 250 L/s has been built in Ensenada to augment the freshwater supply [5]. However, the current demand of 968 L/s, in average, is still not fully satisfied [6]. The case of Ensenada is only an example of the water scarcity situation experienced in the state. An important number of rural communities along the coast face a similar condition and building an RO desalination plant for each of them is neither economically nor technically viable due to limited resources. The lack of clean water makes people vulnerable to infectious diseases such as hepatitis, cholera or typhoid, which in Mexico are considered to be the fifth cause of mortality in infants younger than 5 years [7].

Zarzo and Prats [8] have stated that the minimum theoretical amount of energy required to desalinate seawater with 35,000 ppm of total dissolved solids (TDS) and at 25°C, regardless of the method being employed, is 0.9 kWh/m^3. Additionally, it has been reported that in BC the solar global horizontal irradiation (GHI) determined for the period 1999–2015 exceeds 5.5 kWh/m^2 [9], hence it can be said that there is sufficient solar radiation to meet such energy requirement for desalinating. Also, Pugsley et al. [10] have proposed the use of the following equation to find the degree of applicability (R) of solar desalination in a region:

$$R = \left(\frac{r_N + r_F}{2}\right) r_S r_H \quad (1)$$

where the rank factors r_N, r_S, r_H, and r_F account for the local availabilities of freshwater, saline water, and solar irradiation, plus the level of water stress. They claimed that if in a given region $R > 0.422$, solar desalination is highly applicable. In agreement with their criteria to compute the rank factors, for the state of Baja California $r_N = 0.90$, $r_S = 0.75$, $r_H = 0.77$, and $r_F = 1.0$, which results in $R = 0.55$ from Eq. (1), indicating that BC possesses ideal conditions for solar desalination. In fact, in the neighboring state of Baja California Sur (BCS), with similar climate conditions to BC, the ability of solar stills (SS) to produce enough freshwater to cover the drinking needs of small and isolated communities was successfully demonstrated in the late 1980s and early 1990s with productivities ranging from 1.0 to 3.7 L/m^2/d on summer [11].

The main obstacle of RO desalination and other commercial methods, such as multi-stage flash (MSF) distillation and multi-effect distillation (MED), to be used in isolated communities is the elevated energy inputs they need: 3–4 kWh/m^3 for RO, 10–16 kWh/m^3 for MSF and 5.5–9 kWh/m^3 for MED [12]. Moreover, these technologies are developed to operate in continuous mode; thus powering them with solar energy would oblige the employment of energy storage. Furthermore, it is often not possible to locate the desalination plant close to the energy harvesting and storage place. Such technologies are cost-effective only for large and continuous productions of freshwater [13]. This scenario highlights the necessity of developing new solar desalination methods or improving existing ones, such as solar stills, which are devices that evaporate saline water to produce freshwater after condensing the vapor.

Solar stills constitute a great option for isolated communities due to their simplicity, versatility, and ease of scalability. An SS consists of a room with transparent cover and a black-painted metallic basin on its floor containing saline water. As solar radiation passes through the cover, it is absorbed by the basin, increasing its temperature. The basin then heats the water up to evaporation. The vapor formed rises and transfers its heat to the cover, producing condensate which is collected as freshwater. Different types of solar stills can be found in the literature. The single-slope solar still (SSSS) constitutes the simplest configuration, however the double-slope solar still (DSSS) has the advantage of doubling the condensing surface without adding significant complexity to the system architecture.

Solar stills can be easily built with materials that are economic, locally available, and have ease of operation and maintenance. Furthermore, they can handle feedwater with any level of salinity and minimum pretreatment. Nevertheless, they have the drawback of generating low yields of condensate, enough to satisfy drinking requirements but insufficient to meet other needs. The yield can be augmented by increasing the temperature of the saline water, enlarging the involved heat transfer areas, reutilizing the heat of condensation, providing vacuum, doing the condensation externally, or preheating the feedwater [14–16]. To pursue one or more of these, the architecture of the SS can be modified; wick materials or nanoparticles can be put in the basin together with the water, or mechanical items can be included. However, care must be placed on the modifications implemented otherwise increments in complexity and cost can be significant.

1.2. Implementation of mechanical items to improve the yield of a solar still

As long as mechanical items, such as fans, pumps, water heaters, or condensers, are not integrated into the operation, it is said that the still works in passive mode; however when they are integrated, the still works in active mode. For a conventional DSSS in passive mode, Elango and Kalidasa [17] reported a yield of 4.40 L/m^2/d for 1–cm water depth and 4.01 L/m^2/d for 2-cm water depth, both on spring season; for summer and fall, Feilizadeh et al. [18] informed 4.46 and 3.28 L/m^2/d, respectively, both at 2 cm-water depth. Without changing to active mode, the productivity can also be improved by reusing the latent heat of condensation. This is done by means of placing one or more basins on top of either a SSSS or DSSS. Also, besides the single- and double-slope SS, other geometrical configurations have been proposed: pyramid, tubular, hemispherical, stepped, or vertical [14,16]. Since the conventional DSSS is considerably easy to build, operate and maintain, it is the configuration chosen in this work.

To move to active operation, Taamneh and Taamneh [19] installed a fan on the glass cover of a pyramid SS to promote forced convection conditions internally and compared its performance with respect to a similar SS without fan. They claimed that the daily productivity rose from 2.62 to 3.15 L/m^2 (approximately 20%) due to the fan influence. Nevertheless, the use of a fan has also the potential to decrease the water temperature, which is an adverse effect. Kabeel et al. [20] used a fan to drag the vapor from an SSSS to an external condenser; in this way, vacuum inside the still was provided and the condensation area was enlarged. When compared with an SSSS without those items, they argued that the daily yield showed increments between 16.3% (from 8.12 to 9.44 L/m^2) and 53.2% (from 5.60 to 8.58 L/m^2).

To improve the production by augmenting the temperature of the saline water contained in the basin, Madiouli et al. [21] combined an SSSS with a flat plate collector and a parabolic trough collector, and placed a packed bed of glass balls in the basin to store energy during the day and release it at night. Water flowed through the flat plate collector and oil through the parabolic one. Both fluids released their heat to the saline water by means of two serpentines positioned inside the basin. During spring season, they obtained 6.04 kg/m^2 of distilled water during the day and 0.73 kg/m^2 at night (6.77 kg/m^2 in total). During winter, the day and night yields were 2.78 and 0.65 kg/m^2, respectively, making a total of 3.43 kg/m^2. With respect to an SSSS without any item, the corresponding total yields for summer and winter were considerably lower: 2.51 and 1.38 kg/m^2.

The freshwater production can also be enhanced by elevating the temperature of the saline water before entering the SS. This is done through feedwater preheating with solar heaters. For this purpose, Badran and Al-Tahaineh [22] combined an SSSS with a flat plate solar collector, made of seven parallel steel tubes. On the month of October, they achieved a peak distillate production of 3.51 L/m^2/d, 36% more than when the still was operated without feedwater preheating (2.24 L/m^2/d). In another work, Badran et al. [23] claimed an increment of 52% in the yield of a pyramid solar still when coupled with a flat plate collector on the month of May. The yield without the collector was 3.30 L/m^2/d, whilst that with the collector was 5.0 L/m^2/d.

Muthu Manokar et al. [15] compared the performance of a pyramid SS operating in passive and active modes at 1 cm of water depth in spring season. At passive mode, they reported a daily yield of 3.72 kg/m^2. For the active mode, they first operated the still coupled to a solar water preheater made of parallel straight copper tubes; then, they replaced the collector for another one made of a spiral copper tube. In both cases, they tested the performance at three different flow rates: 1.4, 2.8, 5.7 kg/h. Also in spring season, for the first configuration, they reported daily condensate productions of 5.58, 4.81, and 4.27 kg/m^2; whilst for the second they obtained 6.35, 5.30, and 4.46 kg/m^2. These values were 12.9% to 41.4% larger than the yield at passive mode. They argued that the spiral heater permitted larger heat transfer rates and contact times between the water and the tube.

The solar stills can also be coupled to photovoltaic (PV) panels and the electric power generated used in the still operation. Kabeel et al. [24] positioned a polycrystalline silicon PV panel next to an SSSS with the same inclination angle. They also put a vertical reflecting surface on top of both systems to enlarge the amount of solar rays reaching them. The electric power generated during daytime was stored and utilized to drive an electric heater installed in the basin at night, thus ensuring continuous 24-h operation. For a testing period between 2 May and 11 August, 2019, they reported daily productivities between 10.63 and 12.09 L/m^2. To compare the performance of the system, they built another SSSS with the same dimensions and tested it in the same period, obtaining significantly lower productions: 4.1–4.35 L/m^2.

Elbar and Hassan [25] placed a monocrystalline silicon PV panel on top of the rear wall of an SSSS and the electricity produced was directly sent to a heater located in the basin. Before being sent to the still, part of the saline water was preheated by using it to cool the PV panel; however care should be taken to prevent the panel corrosion due to salinity. The authors also introduced black steel wool fibers in the basin to improve the evaporation rate. For six successive days of September, the largest yield found was 3.53 kg/m^2, whilst in an identical still operated simultaneously the maximum yield was 2.33 kg/m^2, a value 34% lower.

As it is observed from the literature, the performance of an SS is significantly enhanced by augmenting the temperature of the saline water. This can be done through two mechanisms: preheating the saline water before it is sent to the still or adding more heat to the water once it is in the basin. With the aim to keep a simple design, in this work the option of using a spiral solar preheater was selected here to augment the temperature of the water entering the DSSS being researched. Contrary to the work of Muthu Manokar et al. [15] which worked with a spiral heater made of copper, it was preferred here to build the heater with a black plastic hose to avoid corrosion and reduce costs.

1.3. Use of nanoparticles to enhance the yield of a solar still

In the last years, nanotechnology has been a subject of great interest because of the high impact it is having on different areas, such as chemistry, medicine, materials science, and engineering [26]. Metal oxide nanoparticles are widely used in many fields due to their specific properties, such as transparency, high isoelectric point, biocompatibility, antibacterial effect, photocatalytic efficiency, high thermal conductivity, and high radiation absorptivity, among others, which have promoted their application in a wide variety of everyday life goods [27] and engineering processes, including seawater desalination through solar stills [28–31]. When placed in the basin of an SS, the nanomaterials help to increase the absorption of solar radiation and the heat transfer rate to the water by enlarging the area of contact and the convection coefficient [29].

Elango et al. [32] evaluated the addition of zinc oxide (ZnO), tin oxide (SnO_2), and aluminum oxide (Al_2O_3) nanoparticles to the water of an SSSS until concentrations of 0.1% by weight were reached. They measured the thermal conductivity of the formed nanofluid and found increments of 5.25%, 7.16%, and 10.34%, respectively. Then, they investigated the performance of the still at 1-cm water depth, obtaining daily productions of 3.0 L/m^2 for ZnO, 3.22 L/m^2 for SnO_2, and 3.74 L/m^2 for Al_2O_3. Since the production when nanoparticles were not employed was

2.62 L/m^2, the utilization of these ones permitted yield increments of 12.7%, 18.6%, and 30.0%, respectively. They also noticed that the larger the thermal conductivity of the nanomaterial, the higher the temperature attained by the water.

Sahota and Tiwari [33] did an analytical study of the performance of a DSSS with the saline water loaded with cuprous oxide (CuO), titanium oxide (TiO_2), and Al_2O_3 nanoparticles at concentrations of 0.25%. Additional heating was obtained by recirculating the formed nanofluid through an arrangement of photovoltaic-thermal solar collectors. On a 24-h basis, they claimed that through the use of the CuO, TiO_2, and Al_2O_3 nanostructures, the annual yield can be enhanced 5.3%, 16.1%, and 10.4%, respectively, with respect to the case without nanostructures.

The direct contact between the nanomaterials and the saline water can be avoided without losing the advantage of using them. Kabeel et al. [34] followed this option and painted the radiation absorbing surface of the basin of an SSSS with a mixture of black paint and CuO nanoparticles at concentrations of 10%–40% by weight and investigated its performance in different days of Sep 2014. They also built another still of the same dimensions but without nanostructures for comparison. The daily condensate yields they attained at 10% of CuO concentration ranged from 4.0 to 4.25 L/m^2, which represented increments of 16.4% to 17.6% with respect to those achieved with the other still. Moreover, they said that by elevating the concentration of CuO to 40%, a yield augmentation of 25% was observed. In a second work, Kabeel et al. [35] accomplished a peak distillate production of 6.6 L/m^2/d in a pyramid SS with the absorbing plate coated with TiO_2 and black paint at 0.1% of volume concentration and 1 cm of water depth. When compared with the distillate generated without utilizing TiO_2 nanoparticles, the rise in production was 6.3%.

It has also been mentioned in the literature that the morphology of the nanomaterials plays an important role. The fact that non-spherical nanoparticles have more surface area gives them a significant advantage over spherical ones in terms of heat transfer and homogeneity of distribution in the fluid [31]. Sharshir et al. [36] measured a yield increment of 50.3% as consequence of mixing flake-like graphite nanoparticles with water at a concentration of 0.5% by mass in an SSSS. Tap water was used at a depth of 0.5 cm. They argued that besides the high thermal conductivity of the nanostructures, their large specific area and 3D absorbing structure augmented the absorption of radiation and the area in contact with the water, thus enhancing the convection heat transfer.

In a similar work, Balachandran et al. [37] coated the basin of an SSSS with a mixture of ferric oxide (Fe_2O_3) nanoparticles and black enamel paint at 10% of concentration. The shape of the nanostructures employed was similar to needles with pointed tips. When compared with an SSSS only coated with the paint, they found that the yield increased from 2.86 to 4.39 L/m^2/d (53.5% of increment) for 0.5 cm of water depth, and from 2.07 to 2.20 L/m^2/d (6.3% of increment) for 1.0 cm of water depth. According to the authors, the needle-like form of the nanomaterials was largely responsible for the increment because it ensured that a large surface area was available to trap more solar radiation.

In all of the works reviewed so far, it has been clearly proven that the incorporation of relatively low percentages of nanomaterials to the basin or to the saline water of an SS increases the distillate production to values similar to those achieved with the implementations of mechanical items described in Section 1.2, because the nanostructures boost the absorption of solar energy and the heat transmission to the water, enhancing the evaporation rate in consequence. However, in all of the cases published, only one type of nanoparticle was used in each experiment, and the extra potential represented by using two types of nanoparticles simultaneously was not investigated. In fact, in the field of flat plate solar collectors, it has been already recommended to employ nanofluids made with a blend of two or more types of nanoparticles for further efficiency improvement [38].

Therefore, it is the objective of this work to investigate experimentally the potential that combination of TiO_2, ZnO, and Al_2O_3 nanoparticles have for improving the performance of a conventional double-slope solar still equipped with a solar water preheater of spiral geometry. By mixing the TiO_2 nanoparticles with black paint and applying it on the inner surface of the basin, and by adding either ZnO or Al_2O_3 nanoparticles to the water, it is ensured that a combination of TiO_2 and ZnO or TiO_2 and Al_2O_3 exists, consequently two types of different nanoparticles act on the system simultaneously. Three cases were investigated: DSSS with TiO_2 only (case C1), DSSS with TiO_2 and ZnO (case C2), and DSSS with TiO_2 and Al_2O_3 (case C3). Feedwater preheating was applied in the three cases.

To preserve the uniformity of the nanostructures and to ensure that a morphology promoting large surface areas was reached, it was preferred not to use commercial nanoparticles, contrary to a significant number of the works reviewed. The TiO_2, ZnO, and Al_2O_3 employed here were specifically synthesized for this application through easily scalable methods. Emphasis was placed on keeping a simple SS configuration, which can be easily built, operated, and maintained, adequate for future use in isolated communities; for such reason, from all of the ways in which mechanical items can be a complement to the influence of the nanoparticles, only feedwater preheating was chosen.

2. Materials and methods

A conventional DSSS was designed and built to evaluate the effect of incorporating metal oxide nanoparticles and feedwater preheating on the generation of distilled water. The schematic of a conventional DSSS is shown in Fig. 1, where the main mechanisms of heat transfer are indicated. Incident solar radiation (I) crosses the glass cover and reaches the black-painted metallic basin, increasing its temperature. The basin then heats the saline water by convection (q_{cbw}) until evaporation. The vapor formed rises and transfers its heat to the cover, producing condensate, collected as freshwater. The glass cover makes the function of a condensing surface, and the heat acquired by it is transferred to the ambient by radiation (q_{rga}) and convection (q_{cga}). A small part of the heat absorbed by the basin is lost due to conduction through the insulation (q_{cb}). The rates of

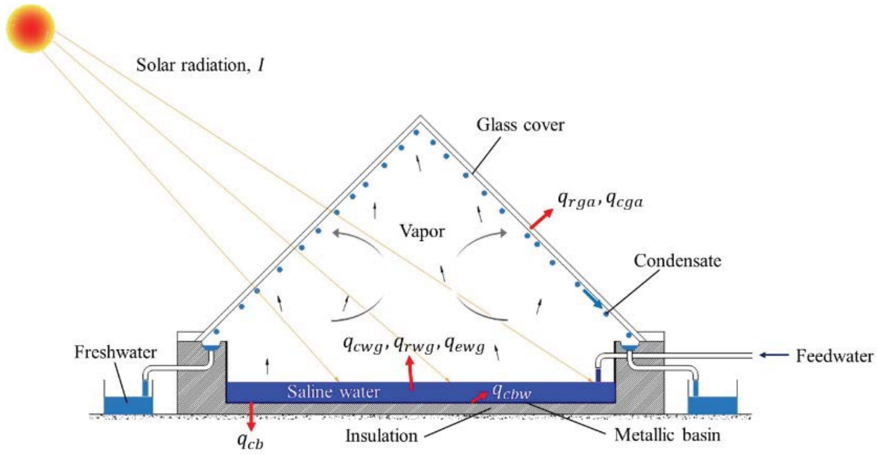

Fig. 1. Schematic of a conventional DSSS with the main heat transfer mechanisms indicated.

heat transfer between the water and the glass by convection (q_{cwg}), radiation (q_{rwg}), and evaporation (q_{ewg}) are:

$$q_{cwg} = h_{cwg} A_w \left(T_w - T_g\right) \tag{2}$$

$$q_{rwg} = h_{rwg} A_w \left(T_w - T_g\right) \tag{3}$$

$$q_{ewg} = h_{ewg} A_w \left(T_w - T_g\right) \tag{4}$$

where h_{cwg}, h_{rwg}, and h_{ewg} are the heat transfer coefficients by convection, radiation, and evaporation, respectively; A_w is the water surface area, T_w is the water temperature, and T_g is the glass temperature. According to Chávez et al. [39] among the three coefficients, h_{ewg} is the most significant. The following equation has been proposed to compute h_{ewg} [40]:

$$h_{ewg} = 16.273\times 10^{-3} h_{cwg} \left(\frac{P_w - P_g}{T_w - T_g}\right) \tag{5}$$

where P_w and P_g are the vapor pressures determined at the temperatures of the water and glass, respectively. The equations to find h_{cwg} and h_{rwg} are [39,41] as follows:

$$h_{cwg} = 0.884\left[T_w - T_g + \frac{\left(P_w - P_g\right)\left(T_w + 273\right)}{268.9\times 10^3 - P_w}\right]^{1/3} \tag{6}$$

$$h_{rwg} = \left(\frac{1}{\varepsilon_w} + \frac{1}{\varepsilon_g}\right)^{-1} \sigma\left[\left(T_w + 273\right)^2 + \left(T_g + 273\right)^2\right]\left(T_w + T_g + 546\right) \tag{7}$$

where ε_w and ε_g are the emissivities of the water and glass, respectively. In this work they were assumed to be 0.96 and 0.88, accordingly [42]. σ is the Stefan–Boltzmann constant (5.67 × 10^{-8} W/m^2 K^4). The correlations to determine P_w and P_g are [43] as follows:

$$P_w = \exp\left(25.317 - \frac{5,144}{T_w + 273}\right) \tag{8}$$

$$P_g = \exp\left(25.317 - \frac{5,144}{T_g + 273}\right) \tag{9}$$

The design of the DSSS constructed is portrayed in Fig. 2. The basin had an inner area of 0.58 m^2 and it was made of aluminum. The surface exposed to solar irradiation and in contact with the saline water was covered with a mixture of black paint and TiO_2 nanoparticles at 1.0% of volumetric concentration. A 25-mm-thick layer of extruded polystyrene was placed below and around the four sides of the basin as thermal insulation. The base of the DSSS was made of 12.7-mm-thick plywood and the structure of 19-mm-thick pine wood. In addition, two 6.4-mm-thick tempered glasses with a measured transmissivity of 95% to solar radiation were used as cover. The total dimensions of the still were 1-m-long, 0.7-m-width, and 0.35-m-height.

The inclination angle of the cover was 32°, which corresponds to the local latitude of Ensenada, BC. It has been reported that by keeping an inclination angle equal to the local latitude the largest productivity is achieved [44]. Since the experiments were done in the northern hemisphere, the still was positioned facing south, on the roof of one of the buildings of the Research Centre CICESE, located in Ensenada. The layout of the solar water heater utilized to increase the temperature of the feedwater before being sent to the still can be seen in Fig. 3a. It consisted of a 12.75-m-long black PVC hose, with an inner diameter of 16.4 mm and mounted on top of a 1.1 × 1.1 m plywood base. Plywood sidewalls and a transparent plastic cover (Fig. 3b) were also attached to prevent cooling from convection with the ambient air.

A tank with saline water fed the spiral heater and the still, compensating for the water removed due to evaporation. With the assistance of a level controller and a 60-W-pump the depth of water in the basin was kept at 1.5 cm, in accordance with the values found in the literature [32,35,36]. The pump worked intermittently. The ZnO and Al_2O_3 nanostructures were applied directly to the saline water in the basin, thus there were no nanomaterials present in the spiral solar heater. A refractometer with 1% of accuracy was employed to measure the salinity

(a) (b)

Fig. 2. 3D view of the solar still assembly (a), and side view of the solar still in operation (b).

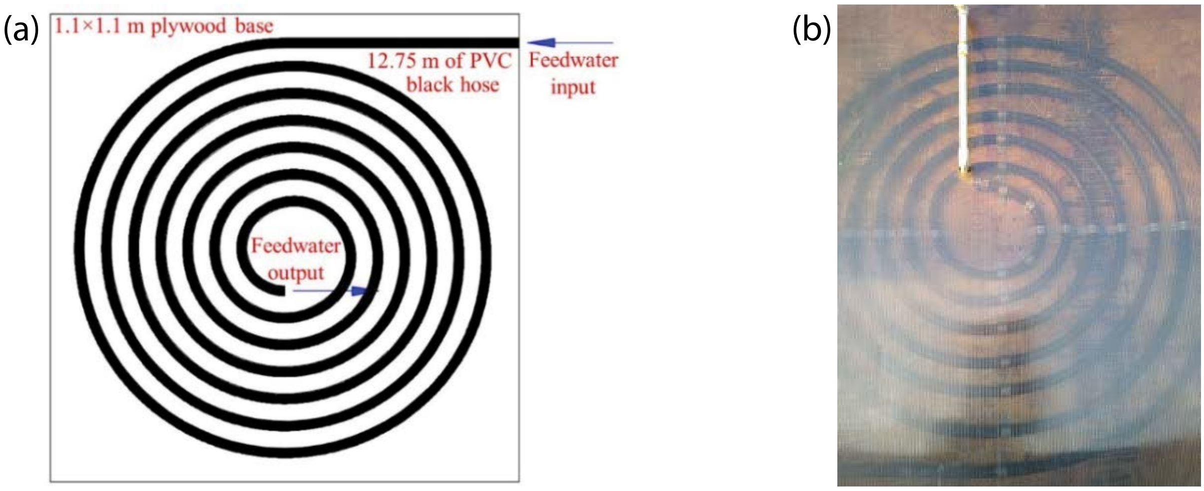

Fig. 3. Layout of the solar water heater (a), and image of the solar water heater in operation (b).

of the feedwater, which was 35%. The accumulation of condensate throughout each experiment was measured with a graduated container with 10 mL of resolution. An in-depth analysis of the distilled water quality was not part of the objectives of this work, however measurements of pH, TDS, and electrical conductivity (EC) were taken to one of the samples to get a broad indication.

Five K-type thermocouples were used to measure the temperatures of the preheated feedwater (T_{fw}), basin (T_b), basin water (T_w), and both glass covers (identified as east side, $T_{g,\text{east}}$, and west side, $T_{g,\text{west}}$). The thermocouples were calibrated using a thermal bath at 15°C, 45°C, and 75°C following the calibration procedure described by Miller [45]. The results are summarized in Table 1. By applying a factor to correct the deviation error on each individual reading during the analysis, the maximum uncertainty of the thermocouples was reduced to 1.1%. The performance of the desalination system was tested during the months of September and October, 2019, on the days shown in Table 2. The evaluation time for each day was from 9:00 to 18:00. In all of the experiments, preheating was used and the operation of the solar still and the solar heater began at the same time. Temperature readings were taken and saved every minute with a data logger.

For each day of experiments, the values of GHI, ambient temperature (T_{amb}) and wind speed (w) were taken from the weather station of CICESE, which measures the variables in intervals of 5 min. Integration was done to compute the hourly (I) and daily (H) solar irradiation. The pyranometer used was a spectrally flat class A pyranometer (consistent with the standard ISO 9060:2018) manufactured by Kipp and Zonen: model CMP11 (Delftechpark 36, 2628 XH Delft, The Netherlands). According to the manufacturer, the maximum uncertainty for daily totals is inferior to 2%. Since the environment conditions varied from one day to another, besides the daily yield, the effect of the nanoparticles on the still was also compared through the thermal efficiency, η_d. The efficiency equation used by Kabeel et al. [46] was modified by adding one term in the denominator to include the power consumed by the pump:

$$\eta_d = \frac{m_p h_{\text{fg}}}{3,600H + W_p \Delta t} \tag{10}$$

where m_p is the daily yield expressed in kg/m², h_{fg} is the latent heat of vaporization of the saline water contained in the basin at the average basin water temperature ($T_{w,\text{av}}$), W_p is the power consumed by the pump (60 W), and Δt is

Table 1
Calibration results of the five K-type thermocouples

T_{cal} (°C)	Thermocouple 1		Thermocouple 2		Thermocouple 3		Thermocouple 4		Thermocouple 5	
	B (%)	*A* (%)	*B* (%)	*A* (%)	*B* (%)	*A* (%)	*B* (%)	*A* (%)	*B* (%)	*A* (%)
15.0	–2.2	±1.1	2.6	±1.1	1.7	±1.1	2.7	±1.1	1.6	±1.1
45.0	–1.6	±1.0	–0.2	±1.0	–0.8	±1.0	–0.3	±1.0	–0.5	±1.0
75.0	–0.8	±1.0	–0.2	±1.0	–0.5	±1.0	–0.1	±1.1	–0.5	±1.0

Note that *B* is the deviation error and *A* is the accuracy at the given calibration temperature (T_{cal}).

Table 2
Nanoparticle-combinations and days of experiments

Combination	Nanoparticles used (concentration by volume, %)	Days of experiments
C1	Black paint with TiO_2 (1%)	10, 13, 14 Sep 2019
C2	Black paint with TiO_2 (1%) + ZnO (0.2%)	18, 19, 20 Sep 2019
C3	Black paint with TiO_2 (1%) + Al_2O_3 (0.2%)	30 Sep; 2, 3 Oct 2019

Note: Preheating was used in all of the cases.

the total working time of the pump during the day. By monitoring the values of T_{fw}, it was possible to find the values of Δt from the clock of the data logger. m_p was computed from the product of the distilled volume times the saline water density, determined from the correlations given by Nayar et al. [47] and Mostafa et al. [48] with an accuracy of 0.14%. If $T_{w,av}$ is expressed in Celsius (°C), then h_{fg} can be computed through the following correlation [49]:

$$h_{fg} = 2,501.897 - 2.407T_{w,av} + 1.192\times10^{-3}T_{w,av}^2 - 1.586\times10^{-5}T_{w,av}^3 \quad (11)$$

To do an error analysis of the distilled water yield and efficiency, the formulae to estimate the propagation of uncertainty given by Taylor [50] were used. The accuracy of each measuring device employed in the experiments, the precision of the correlations used to determine required thermodynamic properties, and the results of the thermocouples calibration were included in the analysis. The accuracy and ranges of the measuring instruments involved are summarized in Table 3.

Table 3
Accuracy and ranges of the measuring instruments

Instrument	Range	Accuracy
Pyranometer	0–4,000 W/m^2	<2%
Thermocouples (type K)	0°C–100°C	≤1.1%
Graduated container	0–2,000 mL	±5 mL
Data logger clock	–	±1 s
Refractometer	0–100%	1%
pH-meter	0.00–14.00 pH	±0.01 pH
TDS- and EC-meter	0–9,990 ppm 0–9,990 μS/cm	±2%

3. Nanoparticle synthesis and characterization

3.1. Nanoparticle synthesis

The main reason to use Al_2O_3, ZnO, and TiO_2 nano-oxides in this work was their suitable values of thermal conductivity (40 W/m K for Al_2O_3, 29 W/m K for ZnO, and 11.8 W/m K for TiO_2 [32,33]) and low cost. Moreover, they exhibit low toxicity and have the ability to perform an antibacterial treatment to the water [51]. The risk to the environment and human health of nanostructured metal oxides has been extensively studied. The ones employed here have shown biocompatibility and biosafety when applied in biological applications at normal concentration ranges, as well as antibacterial activity [52–56]. Moreover, provided that they do not evaporate at the temperatures at which an SS normally operates (<85°C), it is believed that the risk the nanoparticles represent to human health in this application is low, nevertheless a toxicity test of the condensate produced by the SS should be investigated in future works.

The nanoparticles used in this research were specifically synthesized for this application. A bottom-up approach was employed to grow the metal oxide nanostructures incorporated into the constructed solar still to improve its performance. ZnO and Al_2O_3 nanoparticles were synthesized through the hydrothermal method [57–59], whilst the TiO_2 nanoparticles, were grown by the sol-gel method [27]. All reagents used were of analytical grades, without further purification. The synthesis procedure of each type of nanostructures employed is explained in the following subsections.

3.1.1. Synthesis of ZnO nanostructures

In order to synthesize the ZnO nanostructures, 5.95 mg of zinc nitrate hexahydrate ($Zn(NO_3)_2{\cdot}6H_2O$) (Sigma-Aldrich

98%, Mexico) were mixed with 1 g of hexadecyltrimethyl-ammonium bromide (CTAB) (Sigma-Aldrich 99%, Mexico), as surfactant, 50 mL of ethanol and 50 mL of deionized water under magnetic stirring during 5 min, until the solution became clear. After that, 50 mL of 2 M urea (Sigma-Aldrich 99%, Mexico) were added, drop by drop, to the solution, still under continuous stirring. The obtained solution was transferred to a polytetrafluoroethylene (Teflon)-lined stainless steel autoclave, which was immediately heated in a furnace and maintained at 100°C for 24 h. After the growth, the autoclave was allowed to cool naturally, down to room temperature, and the resulting white powder was washed with deionized water, filtered, and dried overnight in another oven at 80°C. Afterwards, it was placed in a muffle furnace and annealed at 600°C for 3 h, in air atmosphere, to obtain the final ZnO nanostructures. This procedure was repeated until the required amount of ZnO was produced.

3.1.2. Synthesis of Al_2O_3 nanostructures

The Al_2O_3 nanostructures were synthesized by mixing 23 mg of aluminum nitrate nonahydrate ($Al(NO_3)_3 \cdot 9H_2O$) (Sigma-Aldrich 98%, Mexico), used as aluminum source, and 2 g of urea (Sigma-Aldrich 99%, Mexico), used as chelating agent, in 80 mL of deionized water. The solution was magnetically stirred at room temperature for 10 min. The mixture was then transferred to the Teflon-lined stainless steel autoclave and heated to 120°C for 24 h. The precipitate formed was separated by filtration, washed with deionized water, and dried overnight in an oven at 80°C. The dried precipitate was placed in a muffle furnace and calcined at 600°C for 3 h to obtain the final Al_2O_3 nanostructures. This procedure was repeated until the total quantity of Al_2O_3 needed for the experiments was generated.

3.1.3. Synthesis of TiO_2 nanostructures

The sol-gel method was employed to synthesize the TiO_2 nanoparticles, using titanium (IV) butoxide (TNBT) as metal precursor. 20 mL of TNBT were mixed with 16 mL of *n*-butanol (Sigma-Aldrich 99.8%, Mexico), and 100 mL of ethylene glycol (Sigma-Aldrich 98%, Mexico), under mechanical stirring for 1 h to form a white gel. The gel obtained was dried at 260°C for 2 h in order to remove the organic compounds, and then annealed at 600°C for 6 h, in air atmosphere, to obtain the final TiO_2 nanostructures. The method was repeated until the required amount of TiO_2 was produced.

3.2. Nanoparticles characterization

Samples of the synthesized nanostructures were analyzed by scanning electron microscopy (SEM), on a JEOL FIB-4500 SEM at 15 kV (Mexico). The chemical composition was evaluated by X-ray photoelectron spectroscopy (XPS), on a SPECS system equipped with a hemispherical electron analyzer, model PHOIBOS 150 WAL, and a monochromatic X-ray source, model XRC 1000. The Al Kα line (1,486.6 eV) at 200 W was used to excite the photoelectrons. In order to inquire the absorptivity of the nanoparticles to solar radiation, reflectance spectra were taken with a UV-visible spectrophotometer AVANTES, model AvaSpecs-2048, equipped with a light source model AvaLight-DH-S-BAL, in the range of 200–800 nm, fully covering the ultraviolet (UV) and visible parts of the solar spectrum, and a small portion of the infrared (which continues up to 2,500 nm for solar radiation).

4. Results and discussion

4.1. Morphology, composition, and absorptivity of the nanoparticles

SEM images of the ZnO, Al_2O_3, and TiO_2 nanostructures are shown in Fig. 4. Figs. 4a and b show flower-like ZnO nanostructures, with an average diameter of 15 μm and made up of many 2D nanosheets, with a thickness lower than 100 nm. Figs. 4c and d show the morphology of the Al_2O_3 nanostructures. As it is observed, they present clusters of flake-like nanostructures, with sizes between 2 and 5 μm, but flake-thickness on the order of nanometers. The TiO_2 nanoparticles exhibited regular shapes, with thickness between 100 and 300 nm, as seen in Figs. 4d and e. From the images obtained, it can be said that the synthesis methods played a key role on the size and morphology of the nanostructured materials. The non-spherical shapes obtained give the nanoparticles a significant advantage over spherical ones because they permit to enlarge the area, which will be in contact with the saline water for heat transfer when used in the solar still [31,60].

Fig. 5 shows the general XPS survey spectra of the metal oxide nanostructures synthesized. All the spectra showed photoelectron peaks of C 1s (285 eV) and O 1s (531 eV). The signal associated to carbon is attributed to environmental carbon, not residual carbon from the synthesis procedures. For Al_2O_3 nanostructures, two peaks at 74 and 120 eV can be seen; they are attributed to Al 2p and Al 2s, respectively [60,61]. For ZnO nanostructures, the observed peaks are associated to Zn $2p_{3/2}$ (1,022 eV), Zn $2p_{1/2}$ (1,045 eV), Zn 3s (140 eV), Zn 3p (91 eV), and Zn 3d (11 eV) [62,63]. In the case of TiO_2 nanostructures, the spectra show peaks linked to Ti 2s (563 eV), Ti $2p_{3/2}$ (456 eV), Ti $2p_{1/2}$ (462 eV), Ti 3s (61 eV) and Ti 3p (35 eV) [64,65]. The elemental analysis shows the formation of desirable metal oxides nanoparticles, without the presence of impurities from other elements.

To evaluate the radiation absorption of nanoparticles, their UV-visible reflectance spectra, shown in Fig. 6, were used. For ZnO and TiO_2 nanostructures, it was found that they were partly transparent (30%–60%) to visible light, between 800 and 430 nm, and showed high absorption (95% for ZnO, and 90% for TiO_2) in the UV region from 430 to 200 nm. The absorption shift observed between ZnO and TiO_2 nanostructures is related to the band gap energy of the materials, where the ZnO has 3.2 eV and TiO_2 has 3.0 eV [66–68]. On the other hand, the Al_2O_3 nanostructures were mainly transparent, with lower absorption of visible light (400–800 nm), a small absorption band on UV region (400–300 nm), and higher UV absorption (~80%) before 250 nm [69], which enhanced the absorption and transmission of heat when alumina was incorporated to the basin water given its larger thermal conductivity [70]. A reflectance analysis of the paint used to coat the basin was not done in this work, however El-Nady et al. [71] investigated the reflectance of a commercial black paint and found high

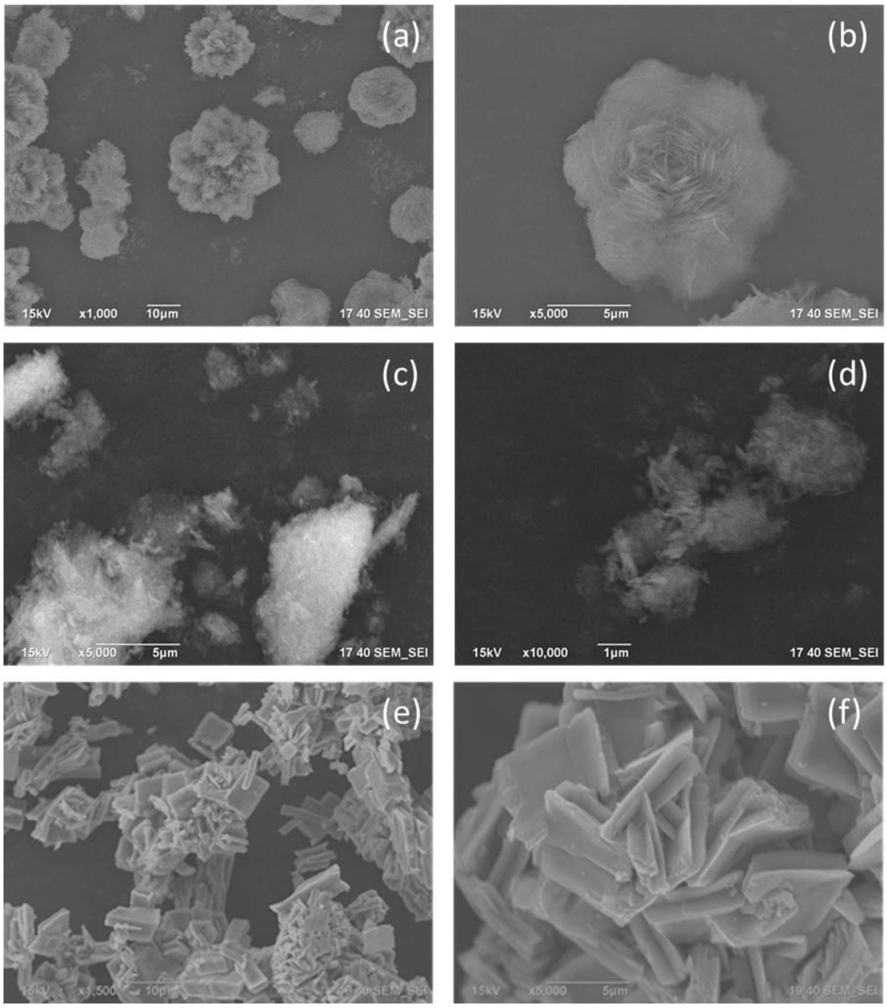

Fig. 4. SEM images of the metal oxide nanostructures: ZnO flower-like nanostructures (a and b), Al_2O_3 flake-like nanostructures (c and d), and TiO_2 regular shape nanostructures (e and f).

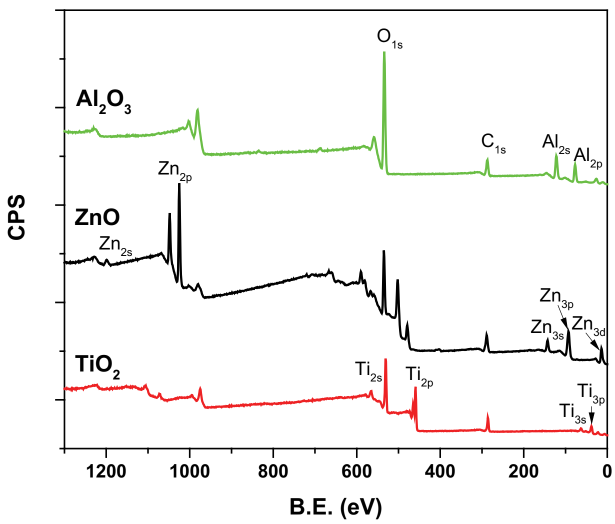

Fig. 5. XPS survey spectra from ZnO, Al_2O_3, and TiO_2 nanostructures. CPS stands for counts per second and B.E. for binding energy in eV.

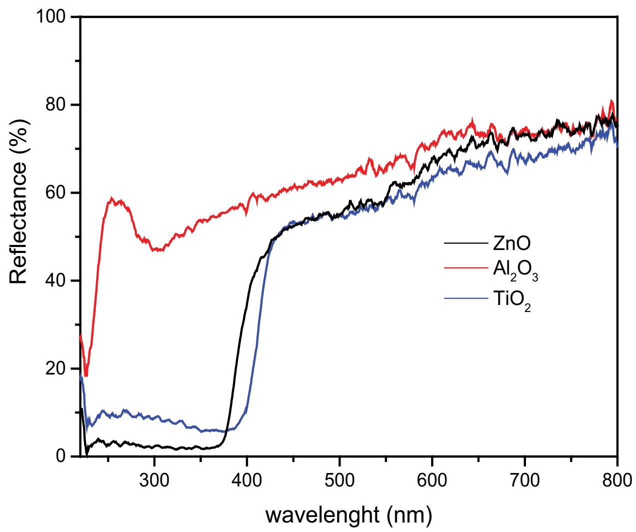

Fig. 6. UV-visible reflectance spectra of ZnO, Al_2O_3 and TiO_2 nanostructures. As the nanostructures are opaque to the incoming radiation 100% – reflectance(%) = absorptivity(%).

absorptivity in the UV-visible region, and moderate in the infrared up to 3,000 nm.

From the spectra results obtained, it can be said that the synthesized nanostructures have the capability of boosting the yield of the DSSS provided that they were proficient enough in absorbing solar radiation at shorter wavelengths, where more energy is being carried. In addition, given the facts that they also possess adequate values of thermal conductivity [32], and enlarged surface areas, as displayed in Fig. 4, it is expected that they improve the heat transfer rate between the basin and the saline water, increasing the temperature of this latter one and promoting a larger temperature difference with the glass cover, thus augmenting the still productivity in consequence [72].

4.2. Effect of using preheating and TiO_2 nanoparticles

According to Table 2 on 10, 13 and 14 Sep 2019, the performance of the DSSS using preheating and TiO_2 nanoparticles was investigated (Case C1). This case is used as basis for comparison. The curves of *I*, T_{amb}, and *w* on the 3 d are plotted in Fig. 7. It can be seen in Fig. 7a that as the day progressed, *I* increased until reaching a maximum around noon time, as expected, then it descended. The irregularity of the curve of *I* for 13 Sep was due to cloud obstructions to beam radiation. The maximum values of *I* reached were 884.83, 883.17, and 859.67 W/m², respectively; and the magnitudes of the accumulated radiation during each day were 6.24, 5.96, and 6.35 kWh/m², respectively.

From Fig. 7b it can be observed that T_{amb} showed relatively similar values on the 3 d before 12:00, afterwards it was appreciably larger on 14 Sep. The highest values of T_{amb} on each day were 22.2°C, 22.0°C, and 25.3°C, respectively. Additionally, it can be noticed in Fig. 7c that *w* did not follow a regular trend on any day and the largest values were measured before 13:00. They were 2.22, 3.12, and 3.16 m/s, respectively. The ambient temperature and wind velocity play a key role in the convection heat transfer from the glass cover to the environment, and though the estimation of the magnitude of such transfer of heat is beyond the scope of this work, from Figs. 7b and c it can be assumed that it was highest on 13 Sep, because T_{amb} tended to be smaller and *w* larger. This positively affects the distillate production.

A comparison of the evolution of T_b, T_w, $T_{g,east}$, and $T_{g,west}$ on the 3 d is depicted in Fig. 8, where it can be appreciated that they followed the trend of *I*, confirming that the solar irradiation is the main driving mechanism of the DSSS. Also, on 14 Sep, the magnitudes of the four measured temperatures were consistently larger, especially after 10:00, which is in agreement with the facts that *H* and T_{amb} were greater on this day and that *w* presented lower values between 11:00 and 16:00, a period of intense solar irradiation. On each of the 3 d, hot saline water from the preheater was delivered intermittently to the basin at temperatures between 30.5°C and 56.3°C to compensate for the evaporated water.

The volume of distilled water per square meter measured every hour and the daily totals are shown in Fig. 9. By employing the accuracies of the measuring instruments listed in Table 3 and the error propagation equations of Taylor [50], the maximum uncertainty obtained for the shown distilled volume amounts was 0.3%. In Fig. 9a, it can be noticed that the rate of distillate production was greater on 10 Sep up to 13:00, afterwards that of 14 Sep dominated. This is explained by the fact that before 12:00 the values of T_w for the 3 d were relatively similar, then the value of T_w on 14 Sep began to be larger, enhancing the evaporation rate in

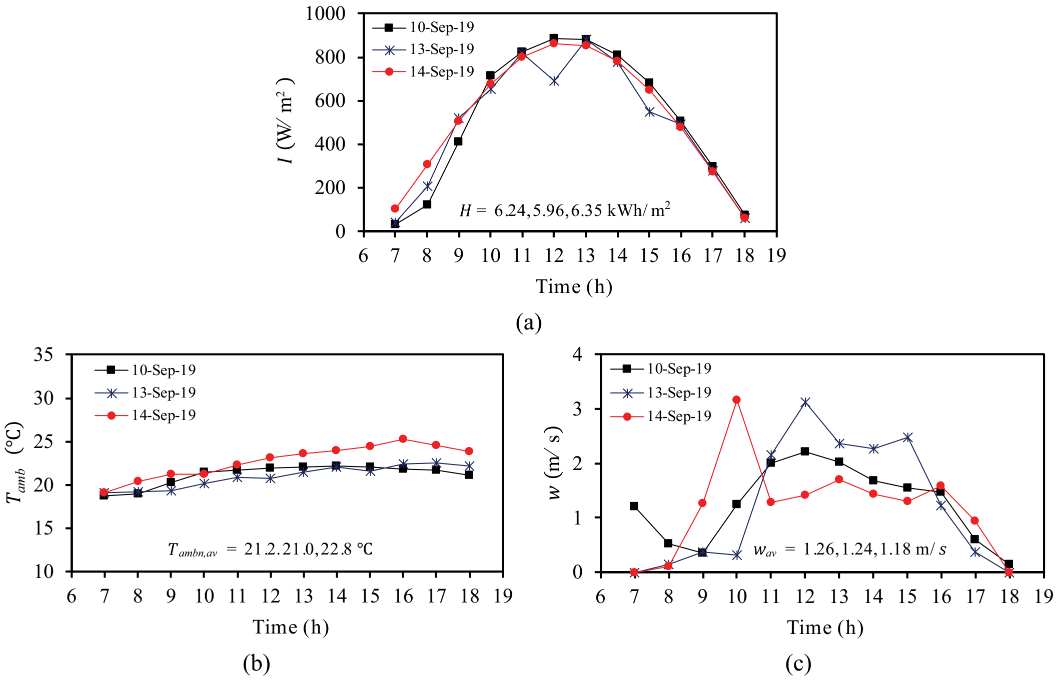

Fig. 7. Hourly solar irradiation *I* (a), ambient temperature T_{amb} (b), and wind velocity *w* (c) during the days corresponding to case C1: preheating and TiO_2. The total solar irradiation *H* and averages of ambient temperature and wind velocity are also shown.

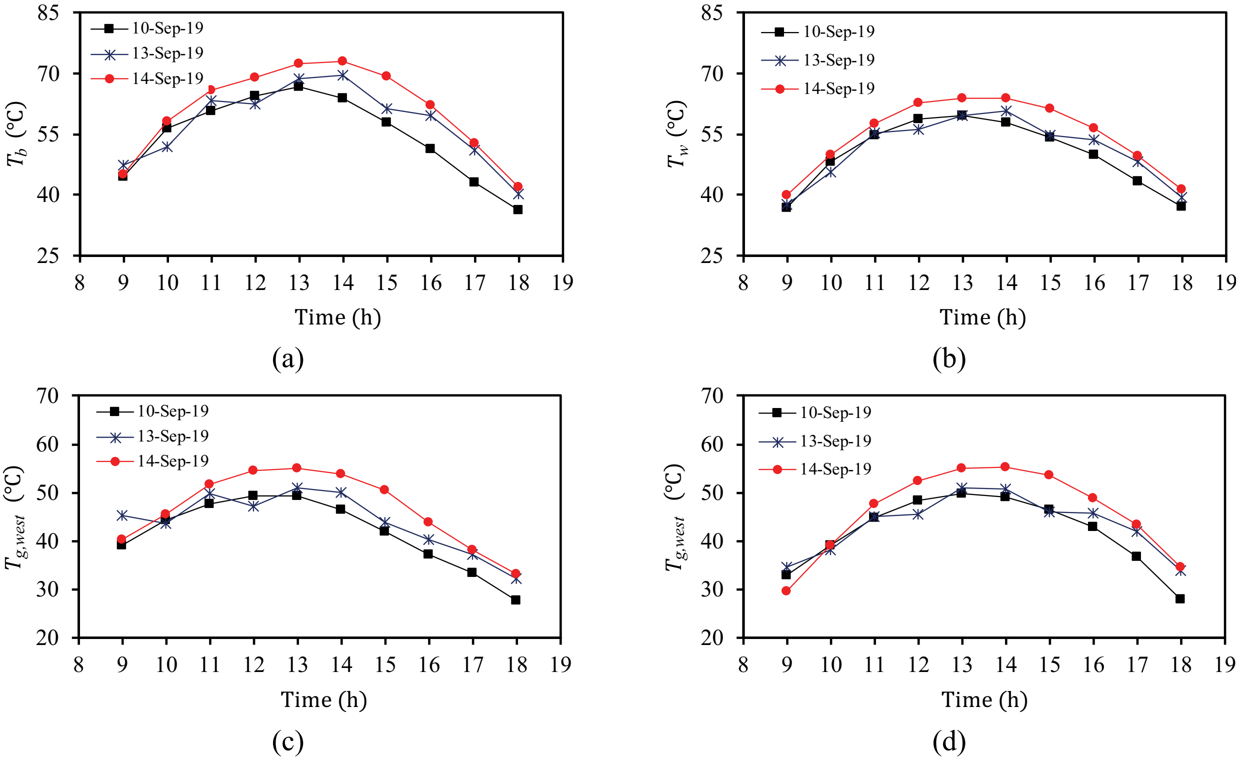

Fig. 8. Variation of the basin temperature T_b (a), water temperature T_w (b), east glass cover temperature $T_{g,east}$ (c), and west glass cover temperature $T_{g,west}$ (d) during the days corresponding to case C1: preheating and TiO_2.

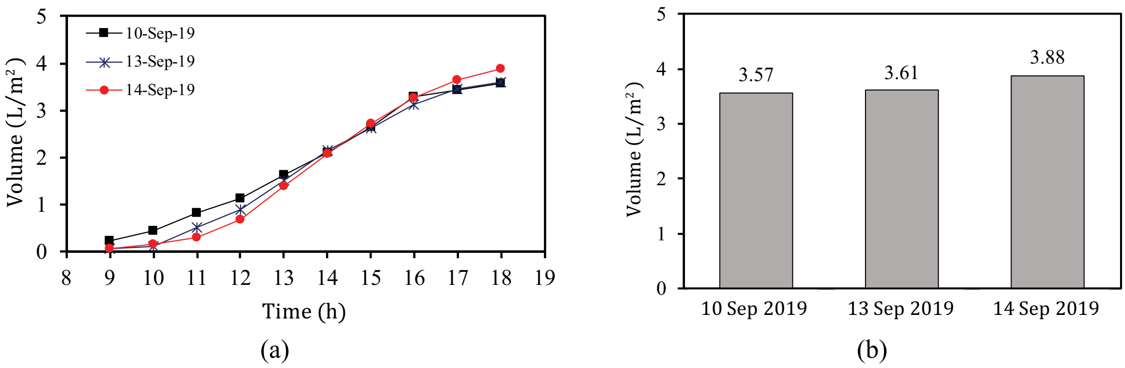

Fig. 9. Cumulative (a) and total (b) yield measured on the days corresponding to case C1: preheating and TiO_2.

consequence. Furthermore, on 14 Sep, the magnitude of w between 16:00 and 18:00 was the largest, improving the external convection with the ambient and the condensation rate.

From Fig. 9c, it can be seen that the maximum production was 3.88 L/m^2 and occurred on 14 Sep. Such yield is slightly higher than the maximum production of 3.7 L/m^2 obtained in 1988 in BCS on summer time using a canal solar still with triangular cross section [11]. The yields of 10 Sep and 13 Sep were noticeably alike due to the fact that from 11:00 to 15:00 greater wind speeds occurred in comparison with 14 Sep. Provided that the largest condensate production of case C1 occurred on 14 Sep 2019, the curves of T_b, T_w, $T_{g,east}$, and $T_{g,west}$ for this day were grouped in one graph, as shown in Fig. 10, to describe the heat transfer processes.

It can be seen in Fig. 10 that the hottest element of the system was the basin, owed to the fact that the capacity to absorb solar radiation of the black-painted metal was boosted by the TiO_2 nanoparticles, which exhibited high absorptivity in the UV region (Fig. 6), where more energy is carried. The appreciable gap between T_b and T_w combined with the wide surface area of the nanoparticles permitted an effective convection of heat between both elements, aiding the evaporation rate. Likewise, the difference between T_w and the cover temperatures successfully promoted the transfer of heat to the glass through convection, radiation,

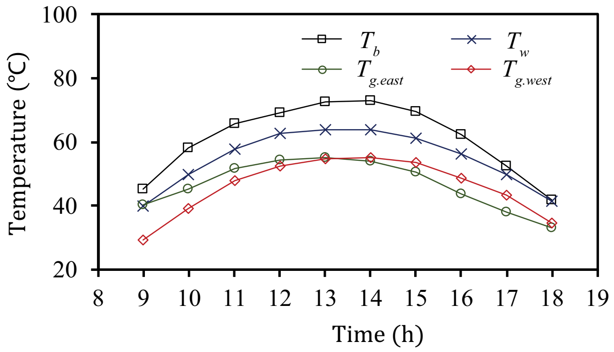

Fig. 10. Variation of the basin temperature T_b, water temperature T_w, east glass cover temperature $T_{g,east}$, and west glass cover temperature Tg,west on the day of largest productivity (14 Sep 2019) of case C1: preheating and TiO_2.

and evaporation, as described in Eqs. (2)–(4), and benefited the condensation rate. The peak values of T_b and T_w, $T_{g,east}$, and $T_{g,west}$ were 73.2°C, 63.9°C, 55.1°C, and 53.7°C, respectively. The way in which the four temperature curves are organized validates the directions of heat transfer illustrated in Fig. 1 for a DSSS. Additionally, and as expected, during the morning, the glass cover facing east had a higher temperature, then after midday the opposite occurred.

4.3. Effect of using preheating and TiO_2 + ZnO nanoparticles

The effect of employing feedwater preheating, TiO_2 nanostructures applied on the basin surface and ZnO nanostructures added to the water contained in the basin (configuration C2 in Table 2) was investigated on 18, 19, and 20 Sep 2019. In Fig. 11, the curves depicting the variations of I, T_{amb}, and w on those days are provided. It can be seen that the differences in I and T_{amb} among the 3 d were practically negligible. More appreciable changes were registered for the wind speed, however a similar trend was observed on the 3 d: a rapid increase from 9:00 to 12:00 followed by a slow decay afterwards, except for 19 Sep. The peak values obtained for I, T_{amb}, and w were 868.42, 845.83, 853.92 W/m^2; 22.2°C, 22.4°C, 21.8°C; and 3.80, 3.10, 3.54 m/s, respectively. With respect to the days of case C1, the values of H were alike, those of $T_{amb,av}$ slightly lower, and those of w_{av} larger.

Given the fact that the environment conditions were considerably similar, the comparison of T_b, T_w, $T_{g,east}$, and $T_{g,west}$ on the 3 d did not add substantially to the analysis, thus it is omitted here. In Fig. 12a, a bar plot with the total yield of distillate is shown. It can be noticed that the maximum yield was obtained for 20 Sep with 4.72 L/m^2. This value is 21.6% larger than the maximum of case C1, demonstrating the potential of using two types of nanoparticles simultaneously to augment the productivity of an SS, because the higher thermal conductivity and absorptivity, in the UV region, of the ZnO (Fig. 6) combined positively with the effect of the TiO_2, successfully complementing each other and improving the heat transfer between the basin and the water.

In Fig. 12b, the variations of T_b, T_w, $T_{g,east}$, and $T_{g,west}$ on the 20 Sep are depicted. The peak values of T_b, T_w, $T_{g,east}$, and $T_{g,west}$ were 70.5°C, 62.6°C, 50.8°C, and 49.3°C, respectively. In this case, feedwater from the preheater was delivered at temperatures between 33.5°C and 55.3°C. Again the temperature curves resembled the trend of the hourly irradiation, thus confirming that this latter one was the variable of maximum influence. By following the same procedure utilized for case C1, the biggest uncertainty obtained for the volumes distilled per unit area of the basin was 0.3%.

In order to compare against configuration C1, the temperature differences between the basin and the water, and between the water and both glass covers for 14 Sep and 20 Sep are plotted in Figs. 13a–c. Additionally, the total heat transfer rate between the water and the cover (q_{twg}), computed with Eqs. (2)–(9), is plotted in Fig. 13d. From Fig. 13a, it can be observed that before 13:00 the difference T_b–T_w was larger for 14 Sep and the opposite occurred afterwards, though with lower magnitude. This occurred because the high absorptivity of both nano-oxides as well as their wide surface area and the bigger thermal conductivity of the ZnO permitted a faster transmission of the absorbed radiation to the water, thus augmenting its temperature.

The influence of the nanoparticles is limited to the basin and the water, promoting the heat transfer between them and bigger values of T_w. The mechanism driving the evaporation and condensation rates is the temperature difference between the water and the glass covers, and as displayed in Figs. 13b and c, such temperature gaps were consistently higher for 20 Sep (case C2). The fact that T_{amb} was lower and w was larger on 20 Sep contributed to reduction in the temperature of the glass and to augment the external convection coefficient; thus more heat could be transmitted from the water to the cover and to the ambient, as illustrated in Fig. 14d, explaining in this way the larger production of distillate obtained for case C2.

4.4. Effect of using preheating and TiO_2 + Al_2O_3 nanoparticles

The influence of the simultaneous utilization of TiO_2 and Al_2O_3 nanostructures on the performance of the DSSS was inquired on 30 Sep, 2 and 3 Oct 2019. The values of the hourly irradiation, ambient temperature, and wind speed corresponding to those days are plotted in Fig. 14. Again, the changes in I and T_{amb} from one day to another were minor, with 30 Sep being slightly colder and the day with more irradiation. On the other hand, marked differences occurred for the wind velocity after 10:00, being also 30 Sep windier. The peaks measured for I, T_{amb}, and w were: 843.0, 835.0, 820.1 W/m^2; 20.8°C, 21.6°C, 21.6°C; and 4.23, 3.72, 2.65 m/s, respectively. In comparison with configurations C1 and C2, the total daily irradiation and T_{amb} were appreciably lower in this case.

In a similar manner to that of C2, the assessment of the changes of T_b, T_w, $T_{g,east}$, and $T_{g,west}$ on the 3 d did not complement the analysis significantly; therefore it is omitted here again. The plot of total productivity on each day is provided in Fig. 15a, with an uncertainty of 0.3%, where it can be seen that the maximum achieved was 5.46 L/m^2, a value 40.5% higher than its equivalent of case C1 and 15.5% higher than that of case C2. Despite the fact that less irradiation was available on 30 Sep, the largest yield was produced because the superior thermal conductivity of the Al_2O_3 nanoparticles

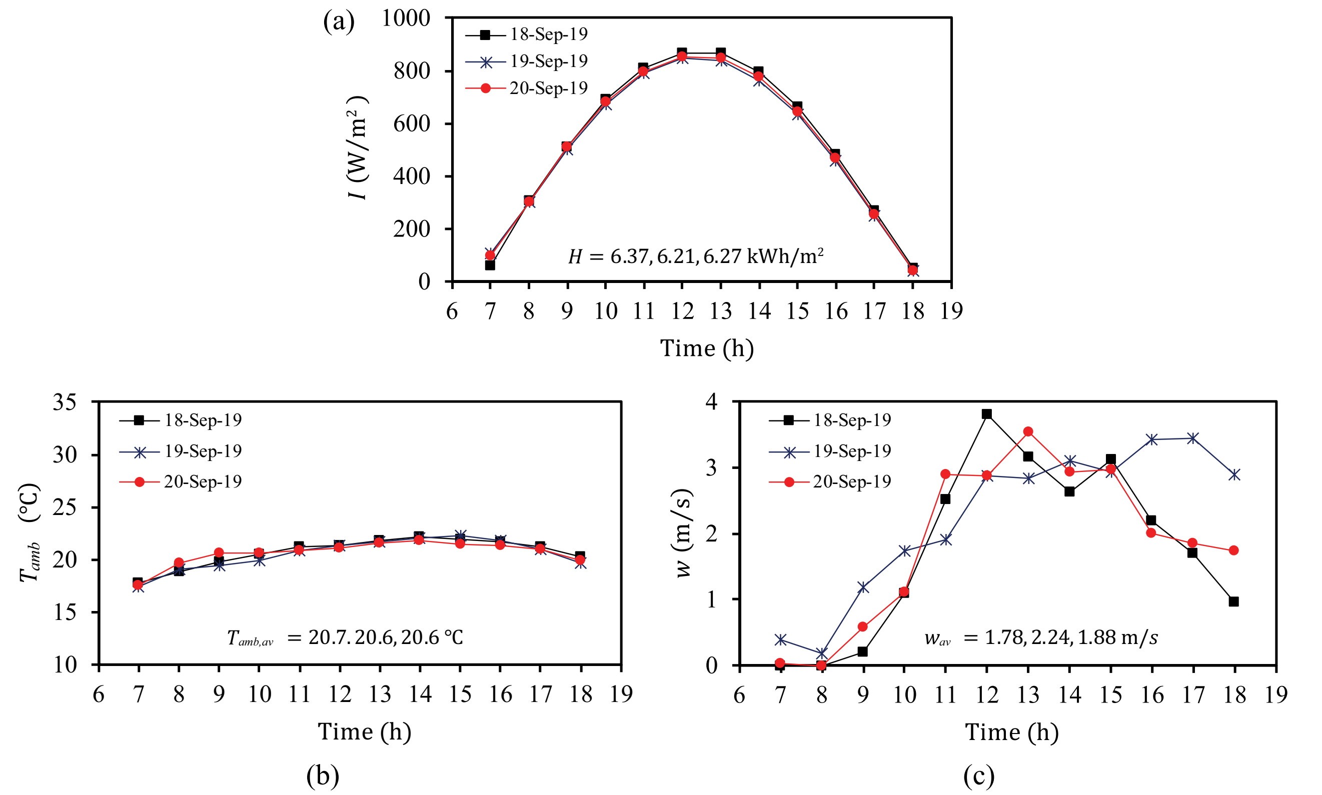

Fig. 11. Hourly solar irradiation I (a), ambient temperature T_{amb} (b), and wind velocity w (c) during the days corresponding to case C2: preheating and TiO_2 + ZnO. The total solar irradiation H and averages of ambient temperature and wind velocity are also shown.

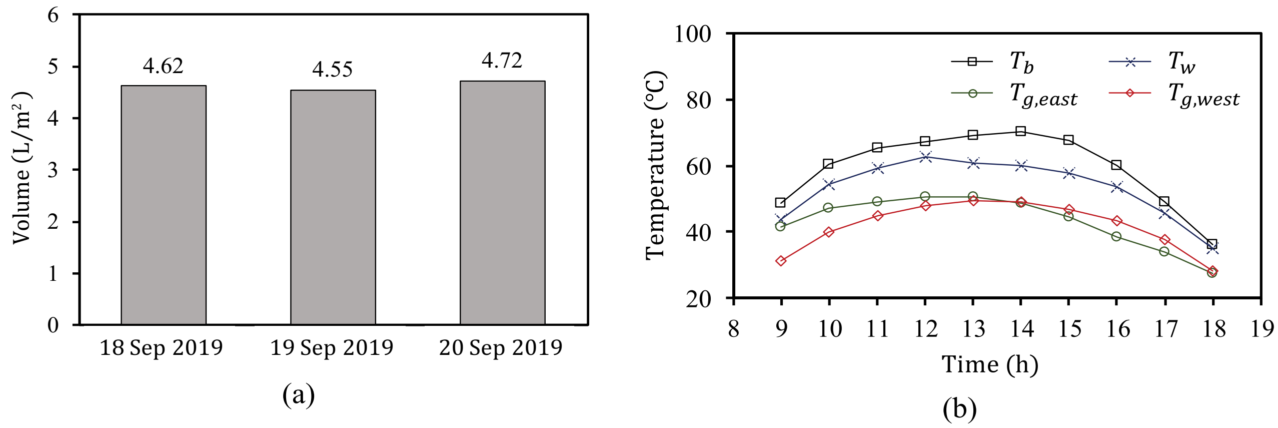

Fig. 12. Total yield (a) and variation of the basin temperature T_b, water temperature T_w, east glass cover temperature $T_{g,east}$, and west glass cover temperature $T_{g,west}$ on the day of largest productivity (20 Sep 2019) of case C2: preheating and TiO_2 + ZnO.

effectively complemented the better capacity of the TiO_2 to absorb solar radiation (Fig. 6) helping to transmit the heat to the saline water more efficiently than in the previous cases [32,33]. Also the flake-like and regular shapes of Al_2O_3 and TiO_2 (Fig. 4) helped to further improve the heat transfer process.

The plots of T_b, T_w, $T_{g,east}$, and $T_{g,west}$ on 30 Sep are given in Fig. 15b. The maximum values recorded for the temperatures of the basin, water, and both glasses were 69.1°C, 62.9°C, 50.2°C, and 49.9°C, respectively. One more time, the tendency depicted by the four temperature curves confirmed that the solar irradiation was the main variable driving the desalination process. The temperature at which feedwater was supplied by the solar preheater varied in the interval 30.3°C–54.8°C. In order to contrast the potential of using the combination Al_2O_3 + TiO_2 with respect to TiO_2 only, the plots

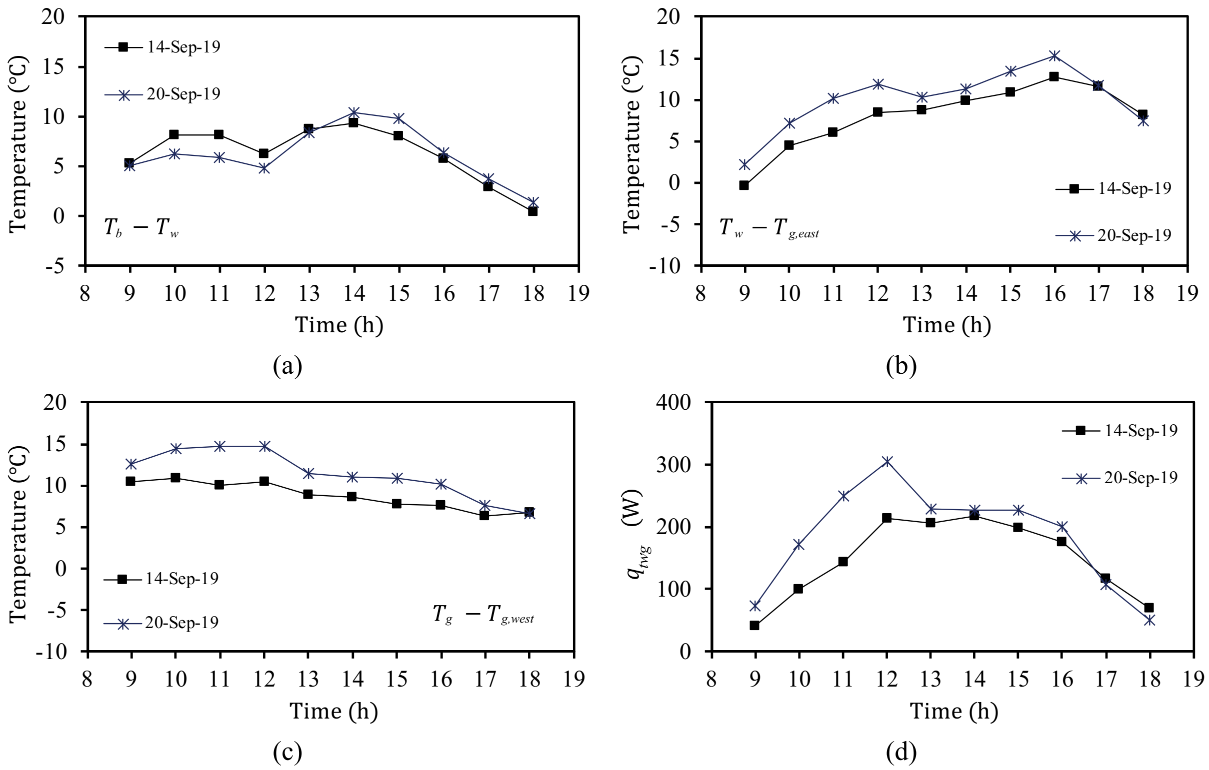

Fig. 13. Differences between the temperatures T_b and T_w (a), T_w and $T_{g,\mathrm{east}}$ (b), T_w and $T_{g,\mathrm{west}}$ (c), and total heat transfer rate between the water and the glass cover (d) for the days of largest productivity of cases C1 (14 Sep, preheating and TiO_2) and C2 (20 Sep, preheating and TiO_2 + ZnO).

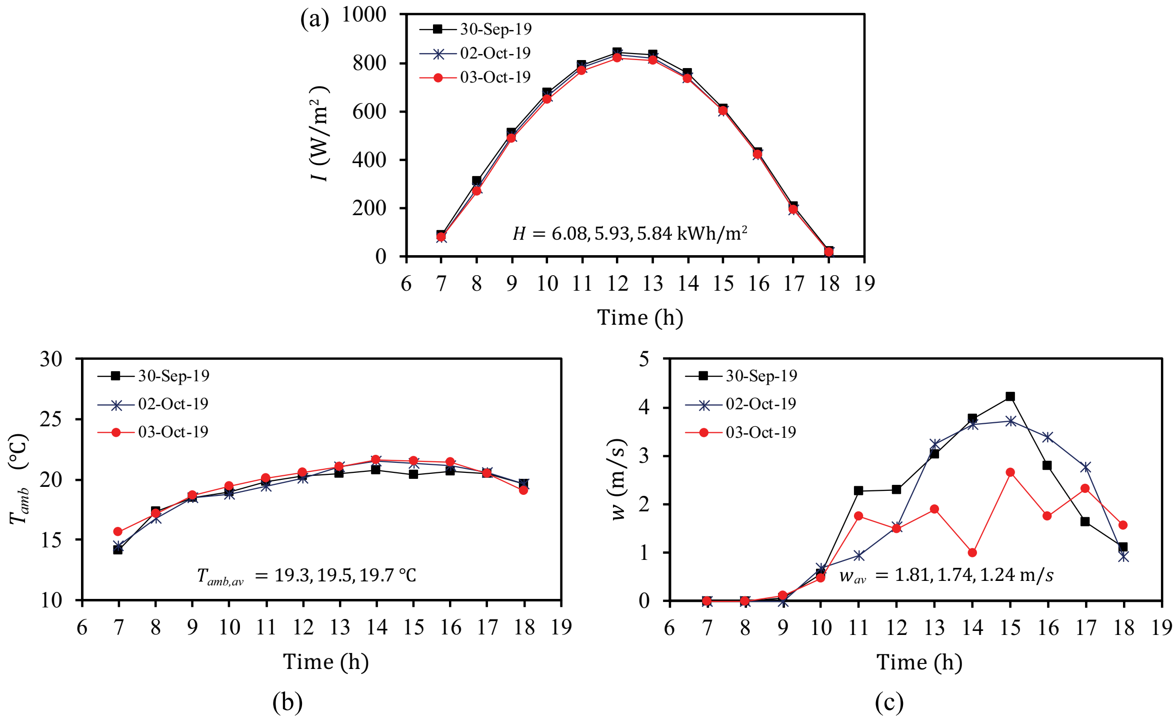

Fig. 14. Hourly solar irradiation I (a), ambient temperature T_{amb} (b), and wind velocity w (c) during the days corresponding to case C3: preheating and TiO_2 + Al_2O_3. The total solar irradiation H and averages of ambient temperature and wind velocity are also shown.

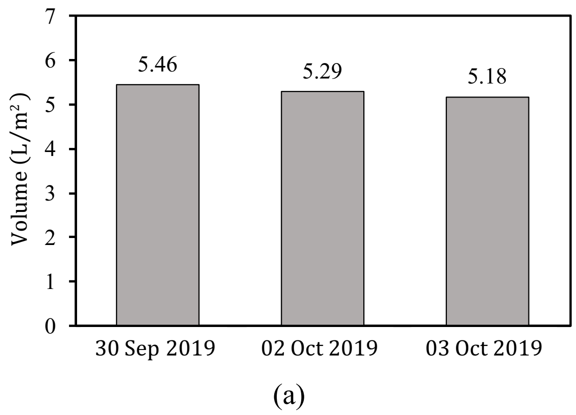

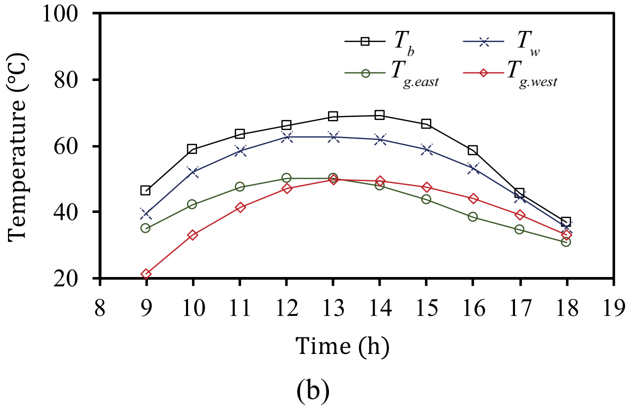

Fig. 15. Total yield (a) and variation of the basin temperature T_b, water temperature T_w, east glass cover temperature $T_{g,east}$, and west glass cover temperature $T_{g,west}$ on the day of largest productivity (30 Sep 2019) of case C3: preheating and $TiO_2 + Al_2O_3$.

of T_b–T_w, T_w–$T_{g,east}$, T_w–$T_{g,west}$, q_{twg} for 30 Sep (Case C3) and the 14 Sep (Case C1), the days of largest yield for each configuration, are given in Fig. 16.

The authors of this work believe that the noticeable lower values of the difference T_b–T_w illustrated in Fig. 16a for Case C3 in contrast to Case C1 are consequence of the superior thermal conductivity of the Al_2O_3 nanostructures with respect to that of the ZnO and TiO_2. A high value of thermal conductivity improves the convection coefficient between the basin and the water, promoting the heat transfer more effectively and causing T_w to rise [29,32]. In addition, the lower ambient temperatures and larger wind speeds measured on 30 Sep caused major temperature gaps between the water and the glass covers, as shown in Figs. 16b and c, enhancing the heat transfer to the cover (depicted in Fig. 16d), and the production of more distillate in consequence.

4.5. Performance comparison

In spite of the fact that the environment conditions were not equal, if the plots of Figs. 9b, 12a, and 15a are contrasted, it can be clearly noticed that the combination of nanoparticles consistently improved the yield of the DSSS with respect to the case where only TiO_2 was employed, and that the best results were attained for TiO_2 plus Al_2O_3. The three configurations investigated can also be compared by means of the thermal efficiency, computed with Eq. (10). The results are plotted in Fig. 17, where the potential of combining nanoparticles to improve the performance of a double-slope solar still is evident. The error bars account for the uncertainty in the efficiency calculations, whose values were determined as suggested by Taylor [50] and are shown at the right of the plot.

The exact comparison of the three cases explored would involve manufacturing three identical stills and preheaters, one for each configuration, and testing them simultaneously. In this way, the three systems would be exposed to the same climate conditions. However, as that approach was not followed in this work due to limited resources, the comparison through the thermal efficiency is also a valid alternative because it includes in the analysis the variation of the solar irradiation from one day to other, which as depicted in Figs. 10, 12b, and 15b is the main variable driving the whole distillation process. Nevertheless, an additional assessment was done by contrasting the maximum yields obtained here with respect to those reported in the literature, for different configurations of SS with and without using mechanical items and nanoparticles. It is shown in Table 4.

For the case of DSSS, it can be observed in Table 4 that the maximum yields achieved here with the combinations of $TiO_2 + ZnO$ and $Al_2O_3 + TiO_2$ nanoparticles were higher than those found in the literature, regardless the employment of nanomaterials or not. For the case of SSSS, larger yields were also obtained, except for the works of Kabeel et al. [20], who employed vacuum and external condensation, Madiouli et al. [21] who provided additional heating to the basin water with a flat plate collector and a parabolic collector, and Kabeel et al. [24] who also provided additional heating with an electric heater connected to a PV panel. Although these mechanical items permit great yield enhancements they also may add considerable complexity and cost to the system in terms of operation and maintenance.

Regarding the pyramid SS type, the productions obtained here were higher only in one case, that of Taamneh and Taamneh [19], however the differences with respect to the other cases were not exceedingly large. When comparing with the works of Badran et al. [23], and Muthu Manokar et al. [15] it is evident that using a solar heater made of steel or copper is more advantageous than using a plastic one, nevertheless those are also subject to corrosion issues. Through this comparison, it is demonstrated that the simultaneous use of two metal oxide nanoparticles and feedwater preheating have the potential to augment the yield of a DSSS considerably without incurring in complex designs, and making use of economic materials.

As mentioned in 2, measurements of TDS, EC, pH, and salinity were taken to one sample of distilled water to get a broad indication of its quality. An in-depth quality analysis was not the aim of this investigation. From the measurements taken, it was found that the water produced with the DSSS had a pH of 4.18, 29 ppm of TDS, 63 μS/cm of EC, and 1%

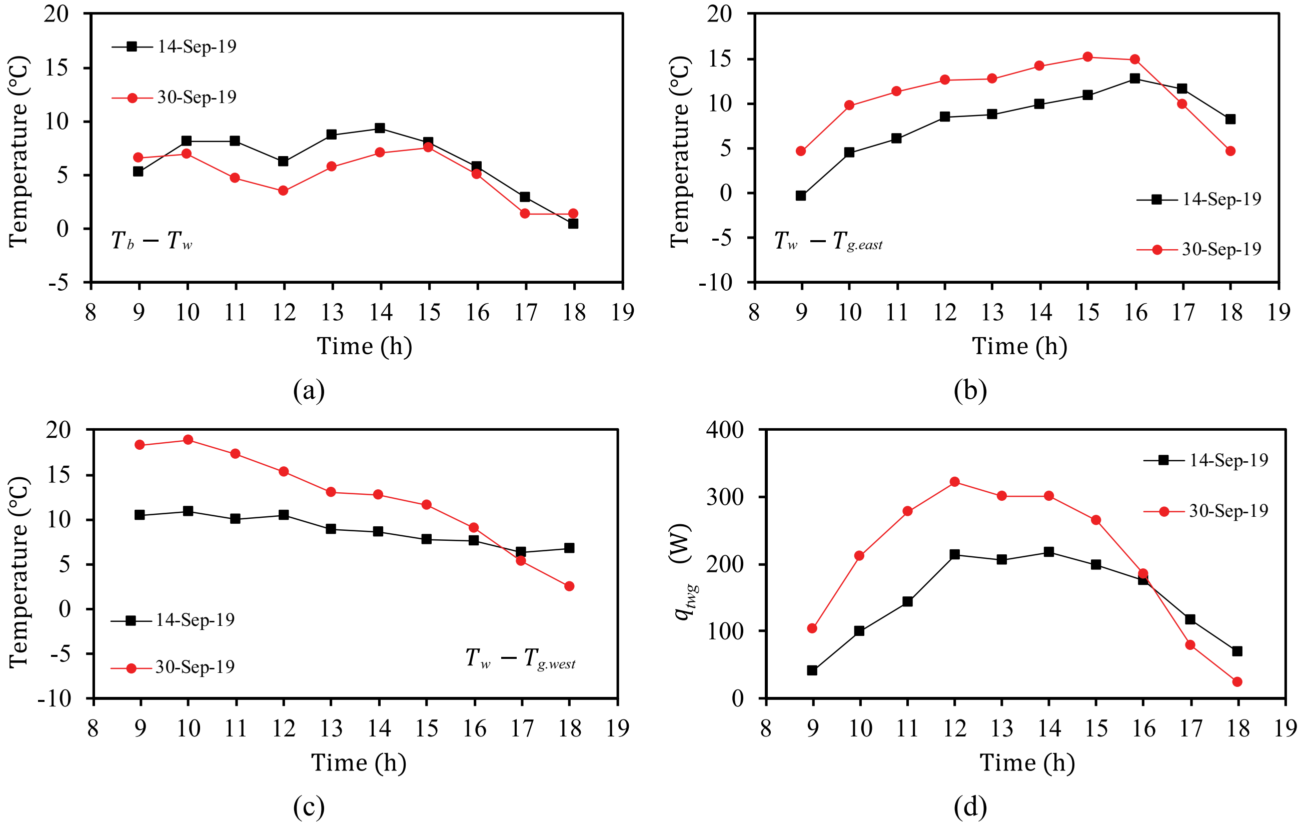

Fig. 16. Differences between the temperatures T_b and T_w (a), T_w and $T_{g,east}$ (b), T_w and $T_{g,west}$ (c), and total heat transfer rate between the water and the glass cover (d) for the days of largest productivity of cases C1 (14 Sep, preheating and TiO_2) and C3 (30 Sep, preheating and $TiO_2 + Al_2O_3$).

of salinity. These values can be contrasted with those of a sample of the tap water supplied to Ensenada: 5.54 of pH; 1,475 ppm of TDS; 3,156 µS/cm of EC; and 6% of salinity.

5. Cost analysis

It was mentioned in Section 1 that the main advantage of solar stills is their simple design, operation, and maintenance. However, since it is a desalination technology recommended to meet at least the basic needs of small and isolated communities, the cost of the produced water has also to be low. In this work, the methodology applied by Kabeel et al. [35] and Elbar and Hassan [25] was followed to determine the cost per liter of distilled water produced. Given the initial investment, including the costs of construction and synthesis of the nanoparticles, the first year cost (FYC) is determined by the following equation:

$$\text{FYC} = \text{CRF} \times \text{initial investment} \quad (12)$$

where CRF, the capital recovery factor, is computed as follows:

$$\text{CRF} = \frac{i(1+i)^n}{(1+i)^n - 1} \quad (13)$$

For the analysis, the annual interest rate i was assumed to be 10% and the number of years of active duty n was 10, since these or similar values are reported in the literature [21,25,31,35,73]. In addition, the annual maintenance cost and salvage value (S) were considered to be 15% of the FYC and 20% of the initial investment [25,35]. Therefore, the following equations can be written:

$$\text{AMC} = 0.15\text{FYC} \quad (14)$$

$$\text{S} = 0.2 \times \text{initial investment} \quad (15)$$

$$\text{SFF} = \frac{i}{(1+i)^n - 1} \quad (16)$$

$$\text{ASV} = \text{S} \times \text{SFF} \quad (17)$$

$$\text{TAC} = \text{FYC} + \text{AMC} - \text{ASV} \quad (18)$$

where SFF is the sinking fund factor, ASV is the annual salvage value, and TAC is the total annual cost. If for each of the combinations of Table 2 an average thermal efficiency is calculated and assumed to be equal throughout the year, the average annual yield of freshwater, P_n, can be computed given the daily GHI measurements. Once P_n is known, the

Table 4
Comparison of the yields achieved here with respect to those of other SS configurations

Author	Type of solar still	Testing place	Season/Month	Water depth (cm)	Daily yield[a] (L/m²)
Elango and Kalidasa [17]	DSSS	India	Spring/March–April	1	4.40
				2	4.01
Feilizadeh et al. [18]	DSSS	Iran	Summer	2	4.46
			Fall	2	3.28
Taamneh and Taamneh [19]	Pyramid SS with fan	Jordan	Summer/June	6	3.15
Kabeel et al. [20]	SSSS with fan and condenser	Egypt	Spring/May	–	9.44
			Summer/June	–	12.56
Madiouli et al. [21]	SSSS with flat plate collector and parabolic trough collector	Saudi Arabia	Spring/May	5	6.77
			Winter/December	5	3.43
Badran and Al-Tahaineh [22]	SSSS with flat plate collector	Jordan	Fall/October	2	3.51
Badran et al. [23]	Pyramid SS with flat plate collector	Jordan	Spring/May	2	5.0
Muthu Manokar et al. [15]	Pyramid SS with straight-tube collector	India	Spring/April–May	1	5.58
	Pyramid SS with spiral-tube collector			1	6.35
Kabeel et al. [24]	SSSS with PV panel and electric heater	Egypt	Spring–Summer May–August	3	12.09 (max.)
Elbar and Hassan [25]	SSSS with PV panel, electric heater and steel wool fibers	Egypt	Summer/September	–	3.53
Elango et al. [32]	SSSS with ZnO nanoparticles	India	Spring/March–April	1	3.0
	SSSS with SnO_2 nanoparticles			1	3.22
	SSSS with Al_2O_3 nanoparticles			1	3.74
Sahota and Tiwari [33]	DSSS with TiO_2 nanoparticles	India	Fall/September	–	2.71
	DSSS with Al_2O_3 nanoparticles			–	2.75
	DSSS with CuO nanoparticles			–	2.89
Kabeel et al. [34]	SSSS with CuO nanoparticles	Egypt	Fall/September	–	4.25
Kabeel et al. [35]	Pyramid SS with TiO_2 nanoparticles	India	Winter/February	1	6.60
Balachandran et al. [37]	SSSS with Fe_2O_3 nanoparticles	India	Winter/January	0.5	4.39
				1	2.20
Present study	DSSS with spiral collector and TiO_2 nanoparticles	Mexico	Summer/September	1.5	3.88
	DSSS with spiral collector and TiO_2 + ZnO nanoparticles			1.5	4.72
	DSSS with spiral collector and TiO_2 + Al_2O_3 nanoparticles		Fall/October	1.5	5.46

[a]For simplicity, a freshwater density of 1,000 kg/m³ was considered to convert kilograms to liters.

cost of each liter of freshwater produced can be obtained as follows:

$$\text{CPL} = \frac{\text{TAC}}{P_n} \tag{19}$$

Provided that the horizontal irradiation measurements of the year 2019 in Ensenada are known, from Eqs. (12)–(19) the costs per liter of freshwater found were 0.034 US \$/L for case C1 TiO_2, 0.038 US \$/L for case C2 (TiO_2 + ZnO), and 0.035 US \$/L for case C3 (TiO_2 + Al_2O_3). The reason for the costs to be notably alike is due to the fact that in the three cases a concentration of 1% of TiO_2 (the most expensive of the three types of nanoparticles) was used, whilst in cases C2 and C3 the concentrations of ZnO and Al_2O_3 were considerably smaller: 0.2%. The price of the ZnO nanostructures was nearly 50% that of the TiO_2, and the price of the Al_2O_3 was the lowest. The costs of distilled water found here lie in the range of prices reported in the literature for different configurations of solar stills: 0.02–0.8 US \$/L [25,31,35,73].

6. Conclusions

A conventional DSSS was designed and built to investigate the potential of using combinations of two different metal oxide nanoparticles (TiO_2 + ZnO and TiO_2 + Al_2O_3) and feedwater preheating on its productivity and thermal efficiency at the climate conditions of Ensenada, BC. Emphasis was placed on constructing a system with low cost and low consumption of energy that could be used in isolated

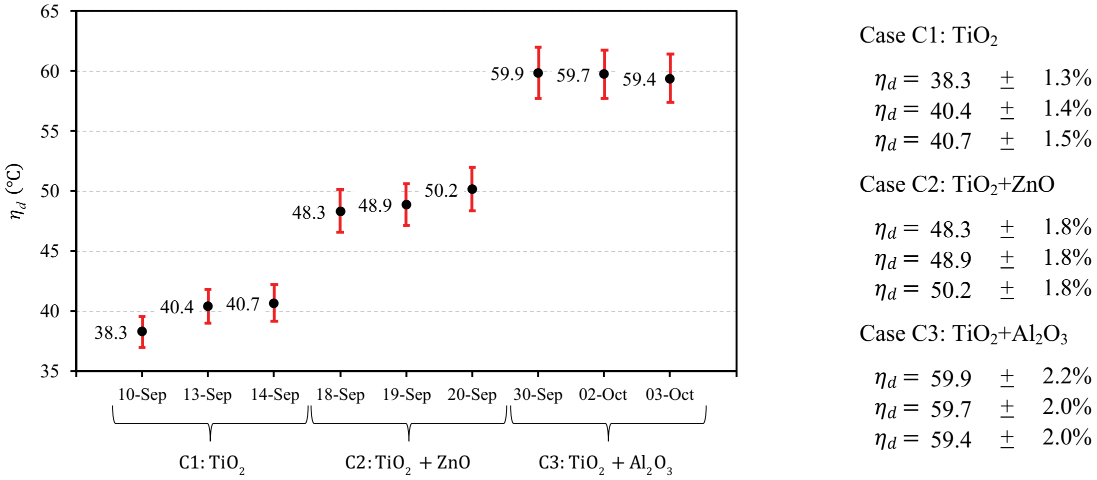

Fig. 17. Efficiency of the DSSS on all of the days of experiments. The uncertainty values are depicted by the error bars and listed at the right of the plot.

communities. The productivities accomplished here with the combinations of nanostructures surpassed those reported in the literature for both SSSS and DSSS assisted with either flat plate collectors or metal oxide nanoparticles only, and were similar or lower than those of pyramid SS equipped with solar collectors or nanomaterials. For the SS configurations where external condensation, parabolic trough collectors, or electric heaters with PV panels were used, the productivities achieved here were inferior. From the nanoparticle characterization and the experiments, the following main conclusions can be drawn:

- The following synthetization methods allowed to produce the required nanostructures with shapes that guaranteed a wide area of contact with the saline water. With the hydrothermal method non-regular shapes were obtained: flower-like for ZnO and flake-like for Al_2O_3. With the sol-gel method regular shapes for TiO_2 were achieved.
- The synthesized ZnO and TiO_2 nanoparticles exhibited a high absorptance of radiation in the wavelength range of 200–430 nm (UV region): approximately 95% for ZnO and 90% for TiO_2. In the interval of 430–800 nm, the absorptance was moderate for both nanomaterials: 30%–60% roughly. In the entire range investigated (200–800 nm), the absorptance of the Al_2O_3 nanostructures varied from 30% to 50% approximately, with the exception of a prominent increment to ~80% at less than 250 nm.
- The maximum yields achieved were 3.88 L/m^2 for TiO_2, 4.72 L/m^2 for the combination of TiO_2 + ZnO, and 5.46 L/m^2 for the combination of TiO_2 + Al_2O_3 at costs between 0.034 and 0.038 US $/L. In all of the cases, there was preheating of the feedwater. The corresponding thermal efficiencies were 40.7%, 50.2%, and 59.9%, respectively, thus demonstrating the advantage of using two nano-oxides simultaneously.
- The high absorptivity of the TiO_2 nanostructures suitably complemented the high thermal conductivity of the Al_2O_3 nanoparticles, thus the largest yields and efficiencies were attained when using them. Nevertheless, provided that the ZnO also has high absorptivity, its combination with TiO_2 is promising too.
- The differences in total daily irradiation and ambient temperature among the days of experiments were not exceedingly large, however changes in the wind speed were noticeable, contributing to greater temperature gaps between the water and the glass cover for the cases where nanoparticle combinations were tested, improving the heat transfer in consequence.

Acknowledgments

The authors of this work would like to thank CONACYT, CICESE, and CNyN-UNAM for the economic support given to this project through the grants FORDECYT 272894 and Basic Scientific Research A1-S-26789 (CONACYT), F0F157 (CICESE), DGAPA-UNAM PAPIIT IN110018 and PAPIME PE210219. The authors would also like to thank D. Domínguez and R. Bonilla for their invaluable technical support.

Abbreviations

A	—	Area, m^2
I	—	Hourly irradiation, W/m^2
h_c	—	Convection heat transfer coefficient, W/m^2 °C
h_e	—	Evaporation heat transfer coefficient, W/m^2 °C
h_r	—	Radiation heat transfer coefficient, W/m^2 °C
H	—	Daily irradiation, kWh/m^2
h_{fg}	—	Latent heat of vaporization, J/kg
m_p	—	Mass of one-day yield, kg
P	—	Pressure, Pa
q_c	—	Convection heat transfer rate, W
q_{cb}	—	Conduction heat transfer rate, W
q_e	—	Evaporation heat transfer rate, W
q_r	—	Radiation heat transfer rate, W
T	—	Temperature, °C
V	—	Specific volume, L/m^2
w	—	Wind speed, m/s

Greek

ε — Emissivity
η_d — Efficiency
σ — Stefan–Boltzmann constant

Subscripts

amb — Ambient
av — Average
b — Basin
fw — Feedwater
g — Glass
w — Water

References

[1] CONAGUA, Estadísticas del agua en México, Comisión Nacional del Agua, Mexico City, 2018.
[2] UN, Managing Water under Uncertainty and Risk: The United Nations World Water Development Report 4, UNESCO, Paris, 2012.
[3] CANACINTRA, Del. Ensenada, Compendio foro de agua Ensenada, BC: problemáticas y soluciones, Cámara Nacional de la Industria de Transformación, Delegación Ensenada, Ensenada, 2014.
[4] CICESE, Agua en Ensenada: más barato, pero persiste la escasez, 2018. Available at: https://centrosconacyt.mx/objeto/agua-en-ensenada/
[5] Proyectos México, Diseño, construcción, equipamiento, operación, mantenimiento y conservación de una planta desaladora en Ensenada, Baja California, 2020. Available at: https://www.proyectosmexico.gob.mx/proyecto_inversion/0839-planta-desaladora-de-ensenada/
[6] Comisión Estatal del Agua de Baja California, Desaladoras del municipio de Ensenada, 2013. Available at: http://www.spabc.gob.mx/wp-content/uploads/2016/08/Desaladoras-Ensenada.pdf
[7] FCEA, Agua en México: un prontuario para la correcta toma de decisiones, Fondo para la Comunicación y Educación Ambiental A.C., Mexico City, 2017.
[8] D. Zarzo, D. Prats, Desalination and energy consumption. What can we expect in the near future?, Desalination, 427 (2018) 1–9.
[9] The World Bank, Solar Resource Data: Solargis, 2017. Available at: https://solargis.com/es/maps-and-gis-data/download/mexico
[10] A. Pugsley, A. Zacharopoulos, J.D. Mondol, M. Smyth, Global applicability of solar desalination, Renewable Energy, 88 (2016) 200–219.
[11] A. Bermudez-Contreras, M. Thomson, D.G. Infield, Renewable energy powered desalination in Baja California Sur, Mexico, Desalination, 220 (2008) 431–440.
[12] N. Ghaffour, T.M. Missimer, G.L. Amy, Technical review and evaluation of the economics of water desalination: current and future challenges for better water supply sustainability, Desalination, 309 (2013) 197–207.
[13] H. Nassrullah, S.F. Anis, R. Hashaikeh, N. Hilal, Energy for desalination: a state of the art review, Desalination, 491 (2020) 114569.
[14] A.A. El-Sebaii, E. El-Bialy, Advanced designs of solar desalination systems: a review, Renewable Sustainable Energy Rev., 49 (2015) 1198–1212.
[15] A. Muthu Manokar, D. Prince Winston, R. Sathyamurthy, A.E. Kabeel, A. Rama Prasath, Experimental investigation on pyramid solar still in passive and active mode, Heat Mass Transf., (2018), https://doi.org/10.1007/s00231-018-2483-3.
[16] T. Arunkumar, K. Raj, D. Dsilva Winfred Rufuss, D. Denkenberger, G. Tingting, L. Xuan, R. Velraj, A review of efficient high productivity solar stills, Renewable Sustainable Energy Rev., 101 (2019) 197–220.
[17] T. Elango, K. Kalidasa Murugavel, The effect of the water depth on the productivity for single and double basin double slope glass solar stills, Desalination, 359 (2015) 82–91.
[18] M. Feilizadeh, M.R. Karimi Estahbanati, A. Ahsan, K. Jafarpur, A. Mersaghian, Effects of water and basin depths in single basin solar stills: an experimental and theoretical study, Energy Convers. Manage., 122 (2016) 174–181.
[19] Y. Taamneh, M.M. Taamneh, Performance of pyramid-shaped solar still: experimental study, Desalination, 291 (2012) 65–68.
[20] A.E. Kabeel, Z.M. Omara, F.A. Essa, Enhancement of modified solar still integrated with external condenser using nanofluids: an experimental approach, Energy Convers. Manage., 78 (2014) 493–498.
[21] J. Madiouli, A. Lashin, I. Shigidi, I.A. Badruddin, A. Kessentini, Experimental study and evaluation of single slope solar still combined with flat plate collector, parabolic trough and packed bed, Sol. Energy, 196 (2020) 358–366.
[22] O.O. Badran, H.A. Al-Tahaineh, The effect of coupling a flat-plate collector on the solar still productivity, Desalination, 183 (2005) 137–142.
[23] A.A. Badran, I.A. Al-Hallaq, I.A. Eyal Salman, M.Z. Odat, A solar still augmented with a flat-plate collector, Desalination, 172 (2005) 227–234.
[24] A.E. Kabeel, M. Abdelgaied, G.M. Mahmoud, Performance evaluation of continuous solar still water desalination system, J. Therm. Anal. Calorim., (2020), https://doi.org/10.1007/s10973-020-09547-5
[25] A.R.A. Elbar, H. Hassan, Enhancement of hybrid solar desalination system composed of solar panel and solar still by using porous material and saline water preheating, Sol. Energy., 204 (2020) 382–394.
[26] M. Nasrollahzadeh, S.M. Sajadi, Risks of Nanotechnology to Human Life, M. Nasrollahzadeh, S.M. Sajadi, M. Sajjadi, Z. Issaabadi, M. Atarod, Eds., An Introduction to Green Nanotechnology, Elsevier, 2019, pp. 323–336.
[27] M. Parashar, V.K. Shukla, R. Singh, Metal oxides nanoparticles via sol–gel method: a review on synthesis, characterization and applications, J. Mater. Sci. Mater. Electron., 31 (2020) 3729–3749.
[28] A.H. Elsheikh, S.W. Sharshir, M.E. Mostafa, F.A. Essa, M.K. Ahmed Ali, Applications of nanofluids in solar energy: a review of recent advances, Renewable Sustainable Energy Rev., 82 (2018) 3483–3502.
[29] K. Khanafer, K. Vafai, A review on the applications of nanofluids in solar energy field, Renewable Energy, 123 (2018) 398–406.
[30] S. Rashidi, N. Karimi, O. Mahian, J.A. Esfahani, A concise review on the role of nanoparticles upon the productivity of solar desalination systems, J. Therm. Anal. Calorim., 135 (2019) 1145–1159.
[31] M. Seyednezhad, M. Sheikholeslami, J.A. Ali, A. Shafee, T.K. Nguyen, Nanoparticles for water desalination in solar heat exchanger, J. Therm. Anal. Calorim., 139 (2020) 1619–1636.
[32] T. Elango, A. Kannan, K. Kalidasa Murugavel, Performance study on single basin single slope solar still with different water nanofluids, Desalination, 360 (2015) 45–51.
[33] L. Sahota, G.N. Tiwari, Exergoeconomic and enviroeconomic analyses of hybrid double slope solar still loaded with nanofluids, Energy Convers. Manage., 148 (2017) 413–430.
[34] A.E. Kabeel, Z.M. Omara, F.A. Essa, A.S. Abdullah, T. Arunkumar, R. Sathyamurthy, Augmentation of a solar still distillate yield via absorber plate coated with black nanoparticles, Alexandria Eng. J., 56 (2017) 433–438.
[35] A.E. Kabeel, R. Sathyamurthy, S.W. Sharshir, A. Muthumanokar, H. Panchal, N. Prakash, C. Prasad, S. Nandakumar, M.S. El Kady, Effect of water depth on a novel absorber plate of pyramid solar still coated with TiO_2 nano black paint, J. Cleaner Prod., 213 (2019) 185–191.
[36] S.W. Sharshir, G. Peng, L. Wu, F.A. Essa, A.E. Kabeel, N. Yang, The effects of flake graphite nanoparticles, phase change material, and film cooling on the solar still performance, Appl. Energy, 191 (2017) 358–366.
[37] G.B. Balachandran, P.W. David, R.K. Mariappan, M.M. Athikesavan, R. Sathyamurthy, Improvising the efficiency of

single-sloped solar still using thermally conductive nano-ferric oxide, Environ. Sci. Pollut. Res., 27 (2020) 32191–32204.
[38] M.E. Zayed, J. Zhao, Y. Du, A.E. Kabeel, S.M. Shalaby, Factors affecting the thermal performance of the flat plate solar collector using nanofluids: a review, Sol. Energy, 182 (2019) 382–396.
[39] S. Chávez, H. Terres, A. Lizardi, R. López, A. Lara, Heat transfer intern coefficient determination in the process of solar still, J. Phys. Conf. Ser., 1221 (2019) 12032.
[40] G. Tiwari, Solar Energy: Fundamentals, Design, Modeling and Applications, Narosa Publishing House, New Delhi, 2004.
[41] R.V. Dunkle, Solar water distillation: the roof type still and a multiple effect diffusion still, Proc. ASME Int. Heat Transf. Part 5, Boulder, 5 (1961) 895–902.
[42] A.E. Kabeel, Z.M. Omara, F.A. Essa, Numerical investigation of modified solar still using nanofluids and external condenser, J. Taiwan Inst. Chem. Eng., 75 (2017) 77–86.
[43] J. Fernández, N. Chargoy, Multi-stage, indirectly heated solar still, Sol. Energy, 44 (1990) 215–223.
[44] A.E. Kabeel, M. Abdelgaied, N. Almulla, Performances of Pyramid-Shaped Solar Still with Different Glass Cover Angles: Proceedings of the 7th International Renewable Energy Congress (IREC), IEEE, Hammamet, 2016, pp. 1–6.
[45] R.W. Miller, Flow Measurement Engineering Handbook, 3rd ed., McGraw-Hill, New York, 1996, pp. 4.1–4.24.
[46] A.E. Kabeel, M. Abdelgaied, A. Eisa, Effect of graphite mass concentrations in a mixture of graphite nanoparticles and paraffin wax as hybrid storage materials on performances of solar still, Renewable Energy, 132 (2019) 119–128.
[47] K. Nayar, M.H. Sharqawy, L.D. Banchik, J.H. Lienhard V, Thermophysical properties of seawater: a review and new correlations that include pressure dependence, Desalination, 390 (2016) 1–24.
[48] H.S. Mostafa, H. John, V. Lienhard, M.Z. Syed, Thermophysical properties of seawater: a review of existing correlations and data, Desal. Water Treat., 16 (2010) 354–380.
[49] H.T. El-Dessouky, H.M. Ettouney, Fundamentals of Salt Water Desalination, Elsevier Science, Amsterdan, 2002.
[50] J.R. Taylor, An Introduction to Error Analysis, 2nd ed., University Science Books, USA, 1997.
[51] S. Stankic, S. Suman, F. Haque, J. Vidic, Pure and multi metal oxide nanoparticles: synthesis, antibacterial and cytotoxic properties, J. Nanobiotechnol., 14 (2016) 73.
[52] S. Gupta, S. Bag, K. Ganguly, I. Sarkar, P. Biswas, Advancements of Medical Electronics, Proceedings of the First International Conference, ICAME 2015, Springer, New Delhi, India, 2015, pp. 193–206.
[53] E. Denes, G. Barrière, E. Poli, G. Lévêque, Alumina biocompatibility, J. Long-Term. Eff. Med. Implants, 28 (2018) 9–13.
[54] A. Sliwinska, D. Kwiatkowski, P. Czarny, J. Milczarek, M. Toma, A. Korycinska, J. Szemraj, T. Sliwinski, Genotoxicity and cytotoxicity of ZnO and Al_2O_3 nanoparticles, Toxicol. Mech. Methods, 25 (2015) 176–183.
[55] E. Baranowska-Wójcik, D. Szwajgier, P. Oleszczuk, A. Winiarska-Mieczan, Effects of titanium dioxide nanoparticles exposure on human health—a review, Biol. Trace Elem. Res., 193 (2020) 118–129.
[56] V. Dincă, A. Mocanu, G. Isopencu, C. Busuioc, S. Brajnicov, A. Vlad, M. Icriverzi, A. Roseanu, M. Dinescu, M. Stroescu, A. Stoica-Guzun, M. Suchea, Biocompatible pure ZnO nanoparticles-3D bacterial cellulose biointerfaces with antibacterial properties, Arab. J. Chem., 13 (2020) 3521–3533.
[57] A.N.P. Madathil, K.A. Vanaja, M.K. Jayaraj, Synthesis of ZnO Nanoparticles by Hydrothermal Method, Proc. SPIE, Vol. 6639, Nanophotonic Materials IV, San Diego, 2007, pp. 66390J.
[58] M. Abdullah, M. Mehmood, J. Ahmad, Single step hydrothermal synthesis of 3D urchin like structures of AACH and aluminum oxide with thin nano-spikes, Ceram. Int., 38 (2012) 3741–3745.
[59] J.A. Darr, J. Zhang, N.M. Makwana, X. Weng, Continuous hydrothermal synthesis of inorganic nanoparticles: applications and future directions, Chem. Rev., 117 (2017) 11125–11238.
[60] T. Song, Q. Liu, J. Liu, W. Yang, R. Chen, X. Jing, K. Takahashi, J. Wang, Fabrication of super slippery sheet-layered and porous anodic aluminium oxide surfaces and its anticorrosion property, Appl. Surf. Sci., 355 (2015) 495–501.
[61] J.S. Lee, H.S. Kim, N.K. Park, T.J. Lee, M. Kang, Low temperature synthesis of α-alumina from aluminum hydroxide hydrothermally synthesized using $[Al(C_2O_4)_x(OH)_y]$ complexes, Chem. Eng. J., 230 (2013) 351–360.
[62] N.R. Panda, B.S. Acharya, Impurity induced crystallinity and optical emissions in ZnO nanorod arrays, Mater. Res. Express, 2 (2014) 15011.
[63] P.T. Hsieh, Y.C. Chen, K.S. Kao, C.M. Wang, Luminescence mechanism of ZnO thin film investigated by XPS measurement, Appl. Phys. A, 90 (2008) 317–321.
[64] G.M. Ingo, S. Dirè, F. Babonneau, XPS studies of SiO_2-TiO_2 powders prepared by sol-gel process, Appl. Surf. Sci., 70–71 (1993) 230–234.
[65] B. Erdem, R.A. Hunsicker, G.W. Simmons, E.D. Sudol, V.L. Dimonie, M.S. El-Aasser, XPS and FTIR surface characterization of TiO_2 particles used in polymer encapsulation, Langmuir, 17 (2001) 2664–2669.
[66] A.V. Vorontsov, A.A. Altynnikov, E.N. Savinov, E.N. Kurkin, Correlation of TiO_2 photocatalytic activity and diffuse reflectance spectra, J. Photochem. Photobiol. A, 144 (2001) 193–196.
[67] R. Dhanalakshmi, A. Pandikumar, K. Sujatha, P. Gunasekaran, Photocatalytic and antimicrobial activities of functionalized silicate sol–gel embedded ZnO–TiO_2 nanocomposite materials, Mater. Express., 3 (2013) 291–300.
[68] M.R. Parra, F.Z. Haque, Aqueous chemical route synthesis and the effect of calcination temperature on the structural and optical properties of ZnO nanoparticles, J. Mater. Res. Technol., 3 (2014) 363–369.
[69] P. Nayar, A. Khanna, D. Kabiraj, S.R. Abhilash, B.D. Beake, Y. Losset, B. Chen, Structural, optical and mechanical properties of amorphous and crystalline alumina thin films, Thin Solid Films, 568 (2014) 19–24.
[70] M.H. Sajid, Z. Said, R. Saidur, M.F. Mohd Sabri, Applicability of alumina nanofluid in direct absorption solar collectors, Appl. Mech. Mater., 699 (2015) 366–371.
[71] J. El-Nady, A.B. Kashyout, S. Ebrahim, M.B. Soliman, Nanoparticles Ni electroplating and black paint for solar collector applications, Alexandria Eng. J., 55 (2016) 723–729.
[72] T. Arunkumar, K. Raj, D. Denkenberger, R. Velraj, Heat carrier nanofluids in solar still–a review, Desal. Water Treat., 130 (2018) 1–16.
[73] A.E. Kabeel, A.M. Hamed, S.A. El-Agouz, Cost analysis of different solar still configurations, Energy, 35 (2010) 2901–2908.